

Exploiting Two-Photon Lithography, Deposition, and Processing to Realize Complex 3D Magnetic Nanostructures

Joseph Askey,* Arjen van den Berg, Sandra Ruiz Gomez, Claire Donnelly, Dirk Grunder, and Sam Ladak*

The integration of two-photon lithography (TPL) with magnetic material processing has opened transformative avenues for designing and realizing 3D functional nanomagnetic systems. This review presents a comprehensive overview of how TPL can be leveraged to fabricate 3D architectures that harness magnetism. The fundamental physics of TPL is examined, and recent advances in voxel engineering, resolution, and throughput are reviewed. Emerging strategies for magnetic functionalization, including physical vapor deposition, electrodeposition, conformal coating, and direct writing of magnetic nanostructures and composites, are thoroughly examined in the context of the functional material systems they enable. Applications in 3D nanomagnetism, such as artificial spin ices for neuromorphics, magnetic racetracks, and magnetic microrobots, are highlighted to demonstrate the versatility of TPL-based fabrication platforms. Finally, a forward-looking perspective is provided, which provides future research directions and associated challenges, including the integration of antiferromagnets, spin-caloritronic materials, and altermagnets, as well as the development of neuromorphic magnetic architectures. In doing so, TPL is positioned as an essential method in the development of technologies based upon next-generation 3D functional magnetic materials.

1. Introduction

Advanced nanofabrication techniques have opened new pathways for the realization of 3D nanoscale architectures with functionalities that exceed what is possible with conventional

planar devices,[1-4] Methods such as focused electron beam induced deposition (FEBID),^[5] electrohydrodynamic redox,^[6] and coupled electric and flow field printing have found particular success in directwriting of metallic nanostructures,[7] particularly FEBID for the realization of 3D magnetic nanostructures, [8–10] Laser-based technologies including projection microstereolithography,[11] continuous phase interface printing^[12] and tomographic volumetric additive manufacturing, [13,14] offer scalable means for realizing organic and hybrid component functional materials over a range of resolutions. Such technologies are thoroughly covered in several important reviews[15-17] and figure-of-merit comparisons.[18] Twophoton lithography (TPL) has emerged as a versatile direct-write fabrication technique[1,2,19] for realizing complex 3D structures with feature sizes that span from micrometers to the nanoscale. By harnessing nonlinear, two-photon absorption of femtosecond laser pulses, TPL enables highly localized polymerization within a

resist, allowing the creation of arbitrary 3D geometries and metamaterials for precise control of mechanical, thermal, electronic, and electromagnetic properties. [2]

Nanomagnetism, the study of magnetic materials subject to 2D nanoscale confinement, has attracted significant attention in

J. Askey, A. van den Berg, S. Ladak School of Physics and Astronomy Cardiff University Cardiff CF24 3AA, UK

E-mail: AskeyJW@cardiff.ac.uk; LadakS@cardiff.ac.uk

S. R. Gomez

ALBA Synchrotron Light Source

CELLS

Cerdanyola del Valles, Barcelona 08290, Spain



The ORCID identification number(s) for the author(s) of this article can be found under https://doi.org/10.1002/adfm.202516383

© 2025 The Author(s). Advanced Functional Materials published by Wiley-VCH GmbH. This is an open access article under the terms of the Creative Commons Attribution License, which permits use, distribution and reproduction in any medium, provided the original work is properly cited.

DOI: 10.1002/adfm.202516383

C. Donnelly

Max Planck Institute for Chemical Physics of Solids

01187 Dresden, Germany

C. Donnelly

International Institute for Sustainability with Knotted Chiral Meta Matter (WPI-SKCM2)

Hiroshima University

Hiroshima 739-8526, Japan

D. Grunder

Laboratory of Nanoscale Magnetic Materials and Magnonics

Institute of Materials (IMX)

École Polytechnique Fédérale de Lausanne (EPFL)

Lausanne CH-1015, Switzerland

D. Grunder

Institute of Electrical and Micro Engineering (IEM)

École Polytechnique Fédérale de Lausanne (EPFL)

Lausanne CH-1015, Switzerland

the last 30 years due to the possibilities of controlling static and dynamic magnetic behavior. [9,20-23] From a technological point of view. 2D magnetic systems have revolutionized data storage devices. The discovery of giant magnetoresistance (GMR) within magnetic multilayers^[24–26] led to the introduction of the commercial spin-valve sensor, providing a means to drastically increase storage areal density in magnetoresistive hard disk read heads.^[27] However, improving storage areal density by reducing the individual magnetic element has reached fundamental physical limitations which are commercially difficult to overcome. Nextgeneration memory devices, such as racetrack memory, [28] have been proposed to circumvent such limitations, which leverage magnetic domain walls as digital bits.^[29] Designing such a device in 3D offers the possibility of ultra-high storage density and ultrafast domain wall motion, providing a means to potentially revolutionize data storage devices. With the advent of advanced fabrication technologies, significant research has shifted toward the study of 3D nanomagnetic systems. 3D geometries, with the increased spatial degrees of freedom and additional curvature and torsion-induced anisotropy terms, allow the existence of complex magnetization textures including curvature-modified transverse domain walls,[30] Bloch point walls,[8,31,32] magnetic hopfions stabilized by geometry, [33-35] and curling states, [36] which are otherwise forbidden in analogous 2D systems. Such 3D magnetization textures have fundamentally different dynamic properties, including ultrafast domain wall motion,[37,38] domain wall transformations in cylindrical nanowires, [39] nonreciprocal spin-wave dispersion, [40-42] and hybridization. [43] 3D fabrication technologies allow direct routes to finely control such complex 3D spin textures, [44-47] frustration-induced states, [48-51] topologically protected configurations, [9,21,52,53] and the associated dynamics, [54-56] as well as realize advanced magnetic devices, [57,58] It is worth that such advances in 3D nanomagnetism are only made possible with the advent of advanced 3D characterization methodologies, [59-67] and micromagnetic modelling software, [68-74] however discussing these is beyond the scope of this present review.

Combining TPL with various deposition and post-processing schemes provides a promising route for realizing functional magnetic materials over a range of technological applications (Figure 1). As already mentioned, TPL provides the opportunity to realize complex 3D lattice architectures for the study of fundamental static, [48,49,51] and dynamic phenomena, [50,75] within frustrated systems. 3D systems are also being explored for highdensity, low-power memory and logic architectures, with a common example of 3D racetrack memory being actively pursued using TPL,[58] where the freedom in design, range of resolutions, and scalability could realize this potential technology as a reality. The flexibility in design, coupled with the biocompatibility and attractive physical properties (e.g., a wide range in Young's modulus as well as extrinsically controlled mechanical properties^[76]) of many commercially available resists, is a huge advantage for microrobotics.[77] Additional functionalization of such resists with magnetic materials (in the form of embedded nanoparticles or coatings) allows for the remote actuation, manipulation, and deformation of such structures in a range of environments using external magnetic fields. [78-81] This shows huge potential in revolutionizing targeted drug delivery, cell manipulation, sensing, and in situ micro-surgery. Finally, 3D magnetic ar-

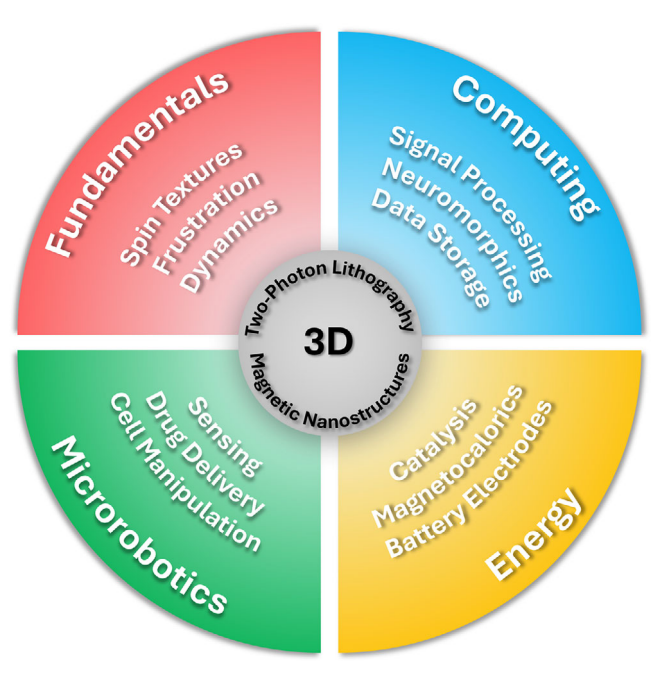


Figure 1. Overview of topics which can be addressed using two-photonlithography and processing in order to realize 3D magnetic nanostructures. TPL allows for realization of structures that enable studies within fundamental magnetism, unconventional computing schemes, energy harvesting and magnetic microrobotics.

chitectures embedded within mechanically or thermally responsive scaffolds may offer applications within energy and harvesting, whereby the massive interfacial area is harnessed for increased magnetoelectric coupling, catalysis, and systems that harness vibrational motion.

This review explores the current state and prospects of TPL for the fabrication of 3D magnetic nanostructures. In Section 2, an overview of the basic principles of TPL is provided, and state-of-the-art TPL research is discussed with particular focus on advancements in resolution and technological scalability. In Section 3, an overview of the methodologies used to deposit or functionalise TPL-fabricated structures with magnetic material is presented, and fundamental insights into the relevant physics discussed. In Section 4, post-processing techniques used to modify TPL produced nanostructures are outlined. Finally, in Sections 5 and 6 we provide a perspective that highlights possible future directions and technological applications, respectively.

2. Principles of Two-Photon Lithography

2.1. Basic Principles

In TPL, a laser is tightly focused (typically diffraction-limited) into a resist with sufficient intensity that two-photon absorption (TPA) is triggered within the components of the resist. Distinct chemical reactions proceed with TPA, depending on the type of resist. For a positive-tone resist, TPA initiates depolymerization via polymer bond scission (Figure 2a), and subsequent development washes away these exposed regions, leaving voids (Figure 2b). For a negative-tone resist, TPA initiates

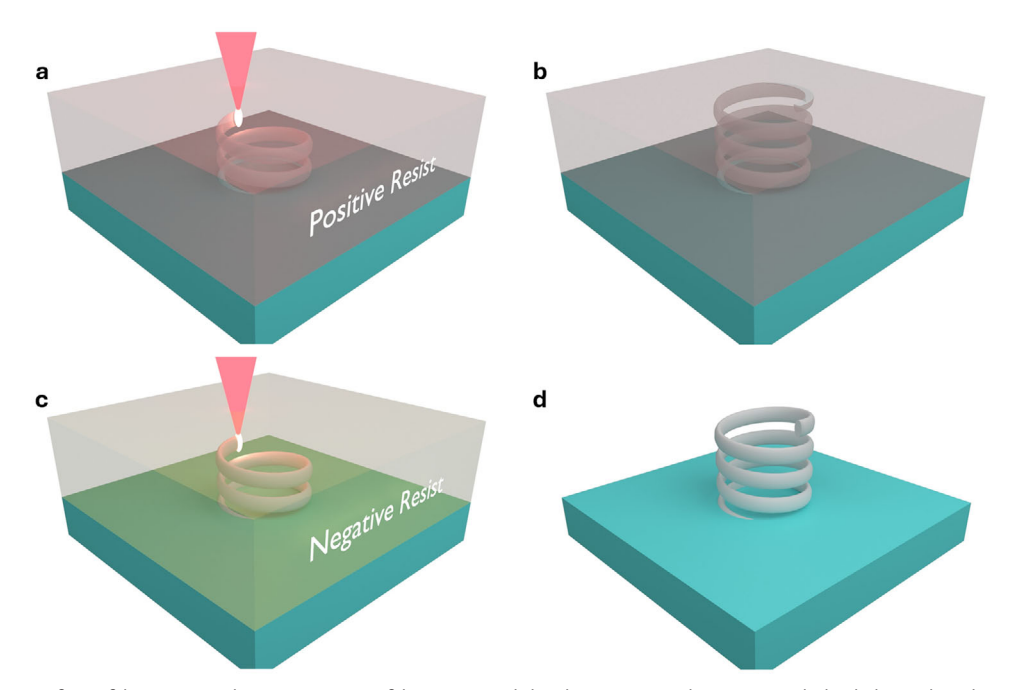


Figure 2. Schematics of TPL fabrication. a–b) Positive resist fabrication and development, resulting in a 3D helical channel. c–d) Negative resist fabrication and development, resulting in a 3D polymer helix.

polymerization via monomer cross-linking of the exposed volume (Figure 2c), and development then removes unexposed regions (Figure 2d).

Due to non-linear absorption, these chemical reactions are confined to the focal volume, referred to hereafter as the voxel (3D pixel analogue). By scanning the voxel with respect to the sample (or the sample with respect to the voxel), one can define arbitrary 3D patterns within the resist. This confinement of the (de)polymerization is a direct result of quadratic scaling (for TPA) for the dose D (and the probability of absorption) with respect to the light intensity I or quartic scaling with respect to the electric field $|\mathbf{E}|$, i.e., $D \propto I^2 \propto |\mathbf{E}|^4$. This non-linear scaling is critical in the suppression of any parasitic dose accumulation local to the voxel and thus in the realization of 3D geometries. [82] For a one-photon absorption process (OPA), the dose scales linearly, and so parasitic dose accumulation leads to the eventual polymerization of regions not confined to the voxel making 3D polymerization effectively impossible.

For the remainder of this section, we will consider a negative-tone resist which undergoes radical polymerization. We also assume the resist polymerizes according to a simple threshold model, where the exposure dose exceeds some specific threshold dose, $D_{\rm th} \leq D_{\rm exp}$. A numerically simulated voxel, plotted as isosurfaces of the threshold dose, is shown in **Figure 3**a for a circularly polarized $\lambda = 780$ nm beam focused through a numerical aperture NA = 1.4 into an immersion medium with refractive index n = 1.518. Lateral and axial profiles in Figure 3b,c illustrate the cylindrical symmetry in the lateral plane, and the ellipsoidal geometry in the axial plane (due to reduced wavevector bandwidth along the beam propagation direction). Lateral and axial line profiles through the voxel are shown in Figure 3d, and the

voxel dimensions are calculated where the region dose exceeds the threshold (red horizontal line, $|\mathbf{E}|^4_{th}=0.8$), with voxel width $l_{xy}=130$ nm, and voxel length $l_z=316$ nm, and voxel aspect ratio $A=l_z/l_{xy}=2.43$.

The voxel width, l_{xy} , and length, l_z , are dependent upon the supplied dose relative to the specific resist threshold. To quantify these dimensions, an ascending scan method, writing simple lines, can be employed. Here, the voxel z-position is sequentially offset with respect to the substrate surface, allowing one to characterize both $l_{x\gamma}$ and l_z .[83,84] For more complex nanostructures, such as interconnected wires and lattices, it is necessary to print arrays of structures where the exposure parameters are varied systematically and then physically characterized, from which optimized writing conditions can be used. The final geometry and the exposure parameters are dependent on a significant number of properties associated with the TPL system (e.g. wavelength, numerical aperture, beam radius at the entrance pupil of the objective lens, immersion configuration, beam polarization), the physical (e.g., viscosity, thermal and mechanical strength) and chemical properties (e.g., photoinitiator and cross-linking monomer types, concentrations and state lifetimes) of the resist. Additional post-printing curing, by way of heat treatment, UV blanket exposures, and careful development procedures^[85] can improve the fidelity and long-term stability of the final prints, with only minor degradation^[86] and changes to the physical and optical properties of manufactured structures.[87]

The lateral, $d_{x\gamma}$, and axial, d_z , resolution of a TPL system, i.e., the minimum resolvable separation between two adjacent written points or lines, is inherently limited by diffraction.^[88] It is directly defined by the excitation beam wavelength λ , the numerical aperture of the focusing lens NA, and, for the axial resolution,

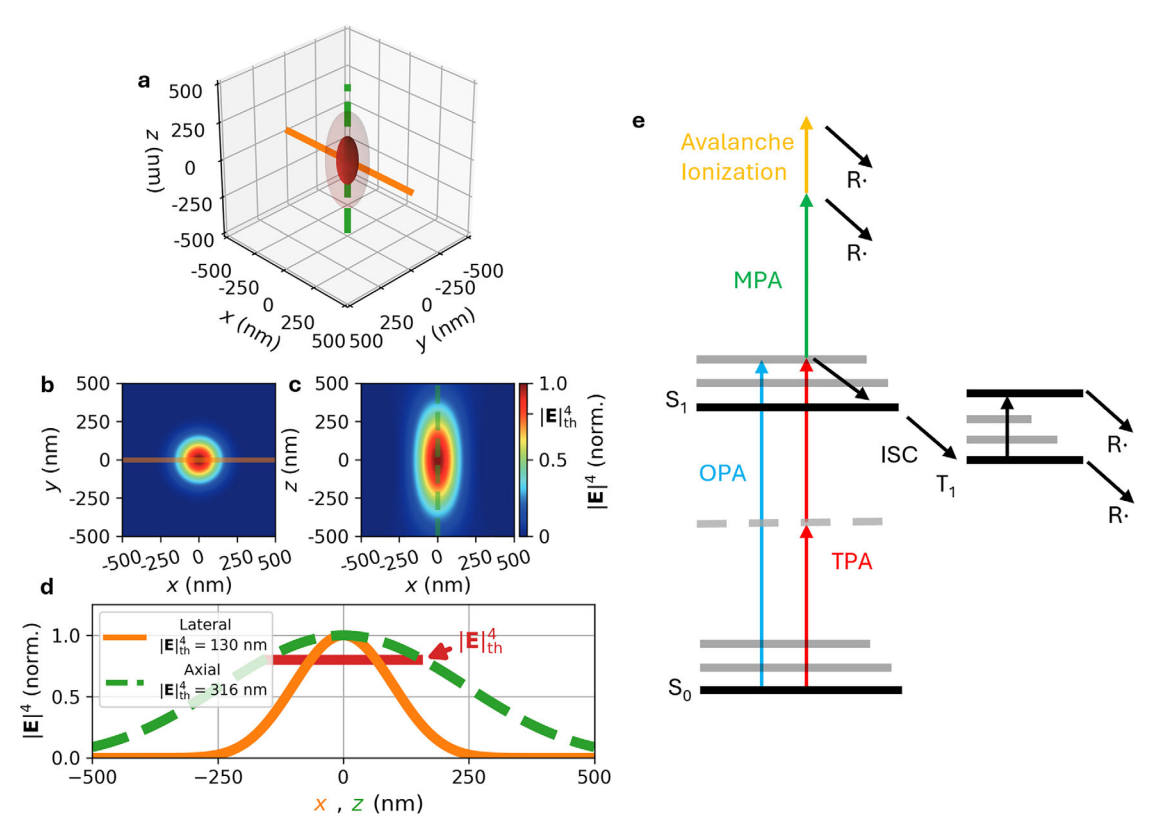


Figure 3. Voxel simulations and simplified Jablonski diagrams. a) 3D voxel represented by threshold isosurface in a diffraction-limited focusing system. b–c) Cross-sections in the z=0 lateral plane, and the y=0 axial plane, respectively, d) Lateral (orange solid) and axial (green dashed) line profiles through the focus showing the voxel dimensions. e) Simplified energy level diagrams illustrating one-photon absorption (OPA), two-photon absorption (TPA), and multi-photon absorption (MPA), from ground (S_0) to excited state (S_1), intersystem-crossing (ISC) to a triplet state (T_1) leading to free radical generation R. MPA at high exposure intensities can lead to avalanche ionization and further free radical generation.

the voxel aspect ratio A, and is given by the two-photon modified Abbe diffraction limit:

$$d_{xy} = \frac{\lambda}{2\sqrt{2} \text{ NA}} \tag{1}$$

$$d_z = \frac{A\lambda}{2\sqrt{2} \text{ NA}} \tag{2}$$

These parameters effectively set the lower limit in spatial lattice parameters of photonic crystals (e.g., woodpiles) and microfluidic channels (e.g., for electrolyte infiltration during electrodeposition).

The polymerization mechanism can be understood using the simplified Jablonski diagram in Figure 3e. Two-photon absorption (TPA) in the photoinitiator molecules leads to an excitation from the ground singlet S_0 state to an excited state S_1 . An inter-system crossing (ISC) from the singlet to a triplet state T_1 leads to bond cleavage and the generation of radical species R-Polymerization proceeds by the chain reaction of monomers and radical species, ceasing once the density of monomer-radical species is depleted in the region of the voxel. [89] MPA can lead to free-radical generation via avalanche ionization, which can also lead to over-exposure when the incident intensity exceeds the optical damage threshold.

To drive efficient TPA, one must employ a sufficiently high photon irradiance to compensate for the otherwise vanishingly small absorption cross-section. [89-91] This is achieved by using high peak power femtosecond pulsed lasers which can provide peak intensities on the order of 1 TW cm $^{-2}$ when focused to a diffraction-limited volume. [1] The beam is focused into the resist, either an oil-immersion configuration with a transparent substrate, or a dip-in method where the focusing lens is directly in contact with the liquid resist. The substrate is then controlled with a three-axis piezoelectric stage for nanoscale positioning with respect to the beam, allowing scan speeds of up to 200 μms^{-1} . TPL systems also make use of galvanometric mirrors, which scan the beam across the field of view of the focusing lens, allowing scan speeds of up to mms $^{-1}$ in the resist.

2.2. State-of-the-Art

TPL is an extremely versatile technology for realizing a diverse range of 3D architectures for various fields of research and technological applications. However, there exists a range of clear challenges, especially in the context of using TPL for realizing functional magnetic nano- and microstructures. Broadly speaking, these fall into three main aspects: 1) resolution and feature size; 2) scalability and throughput; 3) and functionalizing structures



www.afm-journal.de

with various materials, specifically magnetic materials. In this section, the first two will be discussed, and Section 3 will be dedicated to the magnetic material challenges and progress.

2.2.1. Resolution and Feature Size

Commercially available TPL systems typically operate in the infrared with wavelength $\lambda = 780$ nm, limiting the available resolution to around $d_{xy} \approx 200$ nm and $d_z \approx 500$ nm. One route to reducing features is by employing smaller wavelength laser systems, as demonstrated using $\lambda = 405$ nm over 10 years ago by Mueller et al.[92] See Table 1 for a detailed list of resolution and feature size benchmarks with associated exposure and focusing parameters, as well as the corresponding photoresist compositions used. Stimulated-emission depletion (STED) TPL, inspired by superresolution microscopy, has been extensively demonstrated to circumvent resolution limits as well as modify the voxel shape, [88] first pioneered by Fischer et al.[93] In STED-inspired TPL, two co-propagating beams, an excitation and a depletion beam, of different wavelengths are focused into the photoresist. The depletion beam is phase-shaped (e.g., into a donut or bottle-beam profile) to create a central region of zero intensity, thereby suppressing polymerization everywhere except at the focal center. The depletion beam stimulates emission from the excited to the ground singlet state, inhibiting radical generation in the extremities of the voxel.[88,93,94] Gan et al. have demonstrated STED-TPL with lateral resolutions on the order of 52 nm and feature sizes of 9 nm^[95] (Figure 4a), which still stands today as the smallest achieved benchmarks. STED-TPL brings significant experimental complexity both in terms of complex resist formulation^[95] and precise alignment of the beams. [88,93,96] Recently, single-color [97] and quasi-single color STED[98,99] have been demonstrated with sub-150 nm lateral resolutions and sub-100 nm lateral feature sizes, Figure 4b-d respectively. 4Π super-resolution microscopy has also inspired alternative TPL with sub-diffraction resolutions. Here, two counter-propagating beams are focused into a resist and constructively interfere with one another to maximize the axial wavevector bandwidth. Such a 4Π -TPL has been demonstrated by Tičkūnas et al. [100] with voxel aspect ratio A < 1 and axial features of 150 nm (Figure 4e). Experimental complexity with super-resolution TPL (in terms of beam alignment and custom resists for STED, and precise phase and focus matching for 4Π) and cost (in terms of multiple lasers for STED and high-NA objective lenses for 4Π) are high.

Two-step absorption stands as a promising alternative for scalable TPL whilst preserving the smallest resolutions and feature sizes. First demonstrated by Hahn et al.^[90] using $\lambda=405$ nm showed resolutions and features comparable to that of STED-TPL at $\lambda=780$ nm (Figure 4f). Here, the intermediary virtual state is replaced with a real state with well-defined relaxation timescales, circumventing the need for expensive and large footprint femtosecond lasers.^[101] Wider adoption of two-step absorption relies on finding suitable photoinitiating species with several reported for single and two-color, as well as depletion-based two-step absorption,^[102] (Figure 4g) as well as the fundamental absorption mechanisms taking place.^[103] Recent two-color, two-step absorption demonstrations with sub-diffraction resolution and ≈ 50 nm features even with scan speeds of up to 1 mms^{-1[104]}

illustrate that chemical nonlinearities, which otherwise limit feature sizes to slow scanning velocities, can be overcome. Combining two-step single-color absorption with depletion-based mechanisms is a promising route to scalable diffraction-unlimited TPL with large scanning velocities and some of the smallest reported lateral and axial resolutions with sub-30 nm lateral features. [105]

2.2.2. Scalability and Throughput

Industrial-scale adoption of TPL is not yet possible due to several scalability and throughput bottlenecks. First, the reproducibility of structures is adversely affected by the development stage, where large capillary forces can deform and delaminate structures, and anisotropic shrinkage due to insufficient cross-linking during exposures can lead to further structural defects. These effects can be somewhat mitigated using post-exposure UV curing[85,106] or by using critical point driers, the latter of which can cost upward of ≈\$10000. Resist quality, which degrades over time, is critical to the fidelity of the final print as well as the specific exposure conditions required for a given print. For industrial-scale semiconductor processes, resist quality and shelf-life are significantly more advanced compared to TPL-based resists. Significant efforts are devoted to improving the resist quality, reducing the environmental impact, and enabling the recyclability of such TPL-based resists.[107,108] Additionally, standard industrial processes such as lift-off steps and automatic wafer handling are not yet commonplace within

The main limiting factor is that commercial TPL systems typically operate in a serial printing procedure - i.e., single structures written at a given time in a layer-by-layer fashion. The total print rate is then limited by the scanning speed of the sample stage (on the order of µms⁻¹ for piezoelectric stages) or the galvanometric mirrors (on order of mms⁻¹) used to scan the beam, resulting in a typical throughput in the range of 100-1000 voxels s⁻¹ (see Table 1). This can be mitigated with on-the-fly voxel shaping, [109] so-called grayscale lithography, [110,111] or by the adoption of beam parallelization schemes. One such method of beam parallelization is the use of diffractive optical elements (DOEs). Hahn et al.[17] demonstrated a 3×3 array of foci elements with a throughput on the order of $r_{\rm u} \approx 10^6$ voxels s⁻¹, with sub-micron lateral feature sizes but with micron-scale axial feature sizes. Kiefer et al. [112] then demonstrated a 7×7 array of foci elements, improving the throughput by two orders of magnitude whilst maintaining roughly the same feature sizes by Hahn et al. An example of a large volume 3D chiral-roton lattice fabricated using this DOE approach is shown in Figure 4h-i.

Hahn et al.^[113] demonstrated a two-color light-sheet microscopy approach to two-step absorption (discussed in Section 3.2.1), where a combination of light-sheet $\lambda = 660$ nm laser and a projection $\lambda = 440$ nm are focused into a resist, and the solidification only takes place where the combination of the two lasers exceed the polymerization threshold, with example linewidth test structures shown in the angled SEM image in Figure 4j. This work was achieved by the careful design of the resist with a photoinitiator initiator which absorbs light at two specific wavelengths, the first absorption to an idle state and the second absorption to the reactive radical generating state. This



 Table 1. Summary of benchmark work on advancements in TPL.

Refs.	Waveleng	Wavelength (Mode)	A	Resist details		Printing	Printing parameters		Resolution	ntion	Feature size	size	Comments
	λ_1 [nm]	λ_2 [nm]			P_1 [mW]	P_2 [mW]	r_{ν} [voxels s ⁻¹]	Serial/Parallel	d _{xy} [nm]	q_z [nm]	/ _{xy} [mm]	/ _z [nm]	
[92]	405 (C)	ı	1.40	IP-Dip NPI	35.0	I	540	Serial	102 (T) 110 (E)	255 (T) 345 (E)	78 (L) 68 (W)	(NE)	Quasi-continuous wave diode laser
[63]	810 (C)	532 (BB)	1.40	PETA; MEHQ; DETC	7.40	50.0	271	Serial	205 (T) 175 (E)	511 (T) 373 (E)	130 (L)	(NE)	STED-TPL with sub-diffraction limit resolution
[95] Figure 4a	800 (7)	375 (BB)	1.40	SR399 and SR444; BDCC, CQ and EDAB; TED	1.67 × 10 ⁻⁶	7.89×10^{-7}	274	Serial	202 (T) 52 (E)	505 (T) 90 (E)	9 (L) 23 (W)	32 (W)	STED-TPL demonstrating sub-10 nm linewidths
[97] Figure 4b	532 (C)	532 (D)	1.45	TCDA, EO-BPFDA and OPPEA; DETC	4.90	2.00	4281	Serial	129 (T) 140 (E)	324 (T) (NE)	38 (L) 58 (W)	(NE)	Single color aberration-free STED
[98] Figure 4c–d	525 (C)	532 (D)	1.45	TCDA and EBPFDA.OPPEA; DETC; TEMPO; varied quenchers	1.12	9.65	217	Serial	128 (T) 100 (E)	320 (T) (NE)	30 (L) 41 (W)	148 (W)	Proximity-effect free quasi-single color STED
[66]	525 (C)	532 (D)	1.45	PETA; BTPOS; DETC	0.95	9.85	433	Serial	128 (T) 100 (E)	320 (T) 318 (E)	54 (L) 74 (W)	152 (W)	Quenching and depletable photoinitiator quasi-single color STED
[100] Figure 4e	1080 (C)	I	1.40 (1.40)	SZ2080; BIS	0.04	ı	100	Serial	272 (T) (NE)	681 (T) (NE)	200 (L)	150 (L)	First 4 Π -TPL demonstrating voxel aspect ratio A $<$ 1.
[90] Figure 4f	405 (C)	I	1.40	IP-Dip NPI/TMPTA and PETA; benzil; BTPOS	≈0.05	ı	543	Serial	102 (T) 100 (E)	255 (T) 300 (E)	110 (W)	302 (W)	First implementation of two-step absorption
[102] Figure 4g	405 (C)	640 (D)	1.40	Various	Various	ı	Various	Serial	102 (T) (NE)	255 (T) (NE)	(NE)	(NE)	Characterization two-step two-color resists
[104]	405 (C)	532 (C)	1.40	PETA; benzil; BTPOS	0.08	ı	543	Serial	102 (T) 150 (E)	255 (T) 495 (E)	50 (L)	264 (W)	Demonstration of two-step two-color absorption
[105]	525 (C)	532 (BB)	1.45	PETA; benzil; BTPOS	1.50	3.60	1301	Serial	128 (T) 80 (E)	320 (T) 160 (E)	30 (L)	(NE)	Two-step absorption and photoinhibition
[71]	790 (1)	1	1.40	IP-Dip	(NE)	I	9.0 × 10 ⁶	Parallel	199 (T) (NE)	498 (T) (NE)	406 (L)	1010 (L)	DOE 3 x 3 multi-focus TPL with sub-micrometer voxel size
[112] Figure 4h–i	790 (C)	1	1.40	IP-Dip NPI; BBK	19.5	ı	1.4 × 10 ⁸	Parallel	(NE)	498 (T) (NE)	475 (L)	905 (L)	DOE 7 x 7 multi-focus TPL with sub-micrometer voxel size
													(Continued)

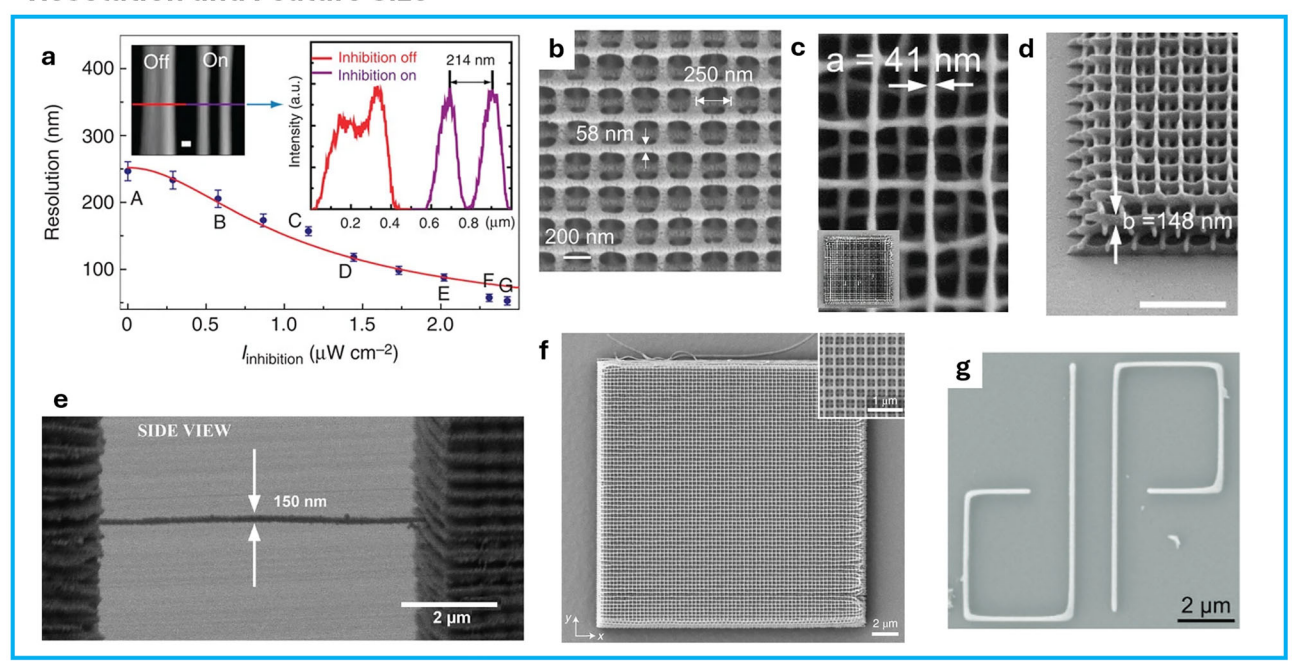
Table 1. (Continued)

Refs.	Wavelength (Mode)	h (Mode)	NA	Resist details		Printin	Printing parameters		Resol	Resolution	Feature size	e size	Comments
	λ ₁ [nm]	λ ₂ [nm]			P ₁ [mW]	P ₂ [mW]	r_{ν} [voxels s ⁻¹]	Serial/Parallel	d_{xy} [nm]	d_z [nm]	(mu] ^{/x} /	/ _z [nm]	
[113] Figure 4j	440 (L)	(7) 099	1.40 (0.13)	TMPTA/PETA/DPEHA; BA; TEMPO	0.02	3.00×10^{3}	7.0 × 10 ⁶	Parallel	111 (T) (NE)	277 (T) (NE)	500 (L)	2200 (L)	Two-color two-step light-sheet printing
[120]	406 (C)	I	1.40	PETA/TMPTA; benzil; BTPOS	0.13	ı	6.1 × 10 ⁴	Parallel	102 (T) 209 (E)	256 (T) 590 (E)	121 (V)	274 (V)	Multi-focus dynamic two-step printing using DMD and holography
Figure 4k	800 (NE)	I	1.49	PETA; BBK	0.41	ı	3.2×10^{6}	Parallel	189 (T) (NE)	474 (T) 1 × 10 ⁶ (E)	200 (W)	2470 (W)	Projection TPL with spatial and temporal focusing using DMD
[115] Figure 4	517 (L)	1	1.49	AR-N-7520	1.00	I	4.0×10^{6}	Parallel	122 (T) 210 (E)	306 (T) (NE)	26 (L)	(NE)	Few-photon TPL with DMD projection
[911]	(7) 008	ı	1.25	PETA; MEHQ; BPADA; TPLPI	96.90	I	3.3×10^{8}	Parallel	226 (T) (NE)	565 (T) (NE)	142 (W)	174 (W)	Projection TPL with spatial and temporal focusing
[117] Figure 4m–n	(7) 008	1	1.3	PETA; TPLPI; BPADA; MEHQ	0.05	I	3.3×10^{8}	Parallel	217 (T) (NE)	544 (T) (NE)	(W) 06	141 (W)	Multi-focus digital holography TPL

Additional objective lenses and corresponding NA are denoted in brackets. Resist details given in terms of product name or in terms of individual monomers; photoinitiators; photoinhibitors; pho (ethoxylated bisphenyl fluorene diacrylate). OPPEA (o-phenyl phenoxy ethyl acrylate). TEMPO (2,2,6,6-tetramethyl-4-piperidyl-1-oxyl). BTPOS (bis (2,2,6,6-tetramethyl-4-piperidyl-1-oxyl) sebacate). SZ2080 (commercial). BIS (4,4-bis (diethylamino)benzophenone). TMPTA (trimethylolpropane triacrylate). BBK ((12,6E)-2,6-Bis(4-(dibuthylamino)benzylidene)-4-methylochokxanone). DPEHA (dipentaerythritol hexaacrylate). BA (biacetyl). TPLPI (4,4-bis (diethylamino)benzylatenone). BPADA (bisphenol A ethoxylate diacrylate). AR-N-7520 (commercial). P_1 = excitation power, P_2 = inhibition or secondary excitation power. Where references quote average intensities ($|\rangle$ or peak intensities $|_p$, powers are then calculated using the relation ($|\rangle$ = $|_p$ Rp $_p$ = TP/III 2 with repetition rate R $_p$, pulse length t_p , transmission factor through the focusing lens assumed to be T = 0.7 unless otherwise stated, and paraxial approximated focal spot $r = \lambda/IINA$, $r_v =$ throughput for parallel TPL configurations. Scanning speeds are converted to r_v by dividing by the paraxial Dip NPI (no photoinitiator, commercial). PETA (pentaerythritol tetraacrylate). MEHQ (4-methoxyphenol). DETC (7-Diethylamino-3-thenoylcoumarin). SR399 (dipentaerythritol pentaacrylate). SR444 (pentaerythritol tetraacrylate) TCDA (tricyclodecane dimethanol diacrylate). EO-BPFDA focal spot size for the specific focusing conditions. $d_{x_0} =$ lateral resolution, $d_z =$ axial resolution, with theoretical (Γ) values calculated using Equations (1) and (2), respectively, and experimental (Γ) values are distinguished. No experimental data denoted by (NE). Ix,, minimum lateral feature sizes, and Iz, minimum axial feature sizes. Values for single lines or line gratings (L) and 3D woodpiles (W) are distinguished. EDAB (ethyl 4-(dimethylamino)benzoate). TED (tetraethylthiuram disulfide). ((1E, 1′E)-(2-((2-Ethylhexyl)oxy)-5-methoxy-1,4-phenylene)bis(ethene-2,1-diyl))bis(N,N-dibutylaniline). BDCC (2,5-bis (p-dimethylaminocinnamylidene) - cyclopentanone). CQ (camphorquinone).



Resolution and Feature Size



Scalability and Throughput

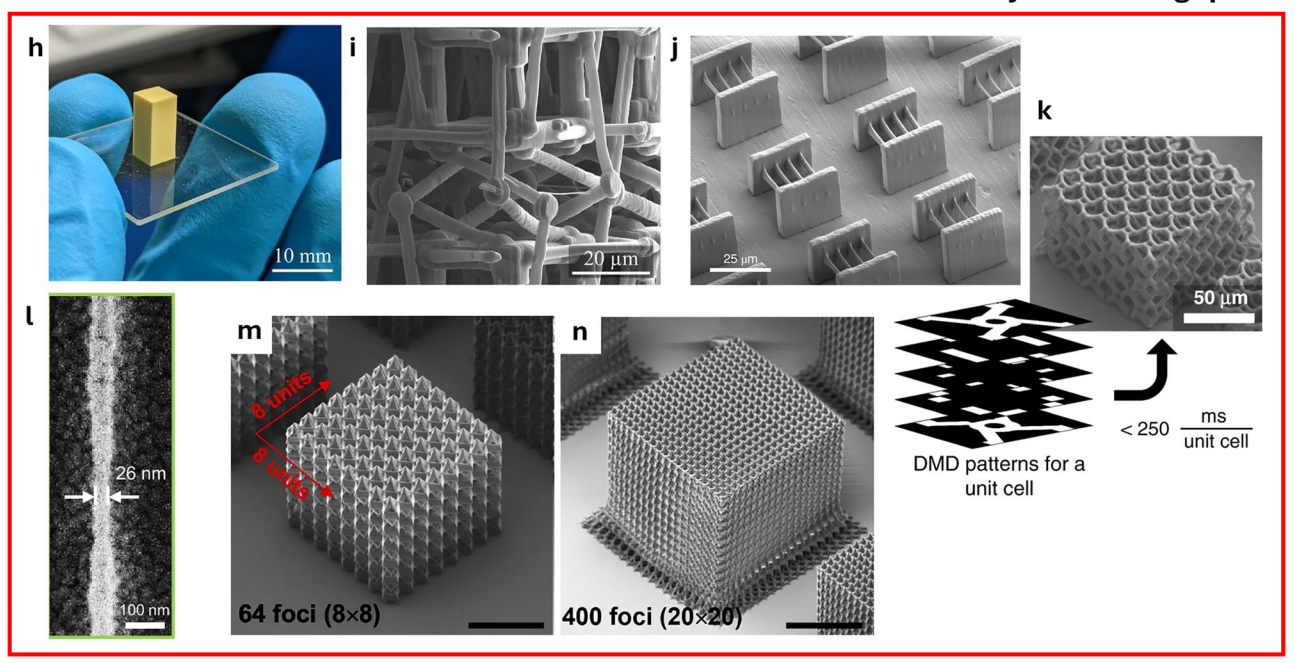


Figure 4. State-of-the-art TPL. a) Resolutions plotted as a function of inhibition beam power, demonstrating a minimum resolution of 52 nm, with insets showing differences in linewidths between standard TPL and STED-TPL. Inset SEM scale bar 100 nm. Reproduced under the terms of the CC-BY 3.0.^[95] Copyright 2013, The Authors, published by Springer Nature. b) SEM of woodpile with 250 nm lattice period and lateral feature of 58 nm, fabricated using single-color STED-TPL. Scale bar 200 nm. Reproduced under the terms of the CC-BY 4.0 license.^[97] Copyright 2022, The Authors, published by Springer Nature. c–d) SEMs of a woodpile fabricated using STED combined with radical quenchers, respectively. Scale bar in (d) 1 μm. Reproduced under the terms of the CC-BY 4.0 license.^[98] Copyright 2024, The Authors, published by Springer Nature. e) SEM of a suspended line using 4Π-TPL. Scale bar 2 μm. Reproduced with permission.^[100] Copyright 2020, AIP Publishing. f) SEM of woodpile lattice fabricated using two-step absorption TPL with lattice period 300 nm. Scale bar 2 μm. Reproduced with permission.^[90] Copyright 2021, Springer Nature. g) SEM view of single line fabricated using two-step STED-TPL. Reproduced under the terms of the CC-BY 4.0 license.^[102] Copyright 2022, The Authors, published by Wiley. h) Optical and i) SEM image of a large chiral-roton metamaterial comprised of over 1×10⁶ unit cells, fabricated via multi-focus TPL. Scale bars 10 mm and 20 μm, respectively. Reproduced under the terms of the CC-BY 4.0 license.^[112] Copyright 2024, The Authors, published by Light Publishing Group. j) SEM of suspended lines fabricated via two-step two-color light sheet TPL. Scale bar 25 μm. Reproduced with permission.^[113] Copyright 2022, Springer Nature. k) SEM of a 3D lattice fabricated via spatiotemporal TPL using a digital micro-mirror device (DMD), with inset binary patterns used to define each printed slice. Scale



www.afm-journal.de

methodology has been demonstrated to reach $r_v \approx 7 \times 10^6$ voxels s⁻¹, but at the expense of a minimum lateral voxel size of 0.5 μ m.

Projection-based TPL with spatiotemporal focusing has been demonstrated in various reports by exploiting digital micromirror devices (DMDs), allowing for simultaneous exposure of layers defined by input binary masks, with Somers et al. [114] reporting on a peak throughput of $r_{\nu} \approx 3\times10^6$ voxels s⁻¹. Such high-throughput parallel-based TPL often compromises resolution and feature size, which can be on the order of microns. Liang et al. reported on the simultaneous improvement of throughput, yielding $r_{\nu} \approx 4\times10^6$ voxels s⁻¹, whilst maintaining sub-30 nm feature sizes by use of few-photon irradiation coupled with digital optical projection [115] (Figure 4n). This work only reports on 2D structures, but marks an important step toward scalable, high-resolution and high-throughput TPL.

Saha et al. report on the spatial and temporal focusing via DMD of fully 3D structures with sub-200 nm features and throughput on the order of $r_{\nu} \approx 3 \times 10^6$ voxels s⁻¹,^[116] demonstrating that feature sizes need not be sacrificed at the expense of speed. Digital holography TPL has been demonstrated allowing for up to 2000 simultaneous laser foci, each with tunable phase, amplitude and position using a DMD with the largest throughput (to the best of our knowledge) of $r_{\nu} \approx 3.33 \times 10^8$ voxels s⁻¹, by Ouyang et al.,^[117] with examples of complex lattices shown in Figure 4m–n. However, diffusion-related voxel expansion was also reported upon drastically reducing the throughput by two orders of magnitude to realize the smallest features, even when using photoinitiators with large absorption cross-sections.

As stated previously, the development of resists is paramount to expanding TPL to an industrial-scale setting. Specifically, the development of radical quenching and scavenging components, [98] an improved dynamic range for repeatable printing processes not subject to over exposures and damage, [90] and additionally to improve the ability to fabricate structures using high speeds and low powers.[112] Understanding the physical and chemical processes that take place in such resists undergoing multi-photon absorption mechanisms is critical to this endeavor.[103] Additionally, more intelligent writing schemes are also necessary to fully exploit TPL as a technology for largescale, high-throughput, and importantly, high-reproducibility 3D nanostructure fabrication. Unveiling and exploiting the underlying phenomena associated with the printing process, such as thermal accumulation, diffusion, and proximity effects, will lead to better-designed writing protocols which can overcome the present challenges faced in TPL.[118] The design of more intelligent and sensitive TPA resists, as well as developing and exploiting more intelligent writing schemes, is a paramount challenge facing this field at present.[119]

3. Magnetic Deposition and Functionalization

When optimizing thin film materials for magnetic technologies, one generally targets either soft or hard magnetic charac-

teristics, i.e., either extremely small or large coercive fields H_c , respectively.[121] These metrics remain important in the design of 3D architectures for specific applications. Soft magnets, whose values $\mu_0 H_c$ reach down to $\approx 5 \times 10^{-7}$ T, are important in the realization of magnetic racetracks, reconfigurable nanomagnetic arrays and systems, where rapid low energy switching and minimal hysteresis are desirable. Hard magnets allow for structures where permanent magnetism is important, such as micromagnetic robotics. All these functionalities would, in general, benefit from a large saturation magnetization M_s of the constituent materials. The reference for record values is the Slater-Pauling limit of $\mu_0 M_s = 2.45 \text{ T.}^{[122]}$ With these points in mind, we now explore the different means to add magnetic functionality to a TPLfabricated structure. The available suite of materials, equipment costs, deposition conditions, and geometries, as well as resolution/feature size limitations, are discussed in **Table 2**:

- 1) Casting a magnetic layer upon a polymeric scaffold via physical vapor deposition, such as thermal evaporation or sputtering, as shown schematically in **Figure 5**a, with an example open-shell cross-section shown in the inset. See Section 3.1.
- 2) Deposition of magnetic material into a polymeric template and subsequent removal, using chemical-assisted deposition schemes such as template-assisted electrodeposition (using both positive and negative resist templates), as shown in Figure 5b, with a solid geometry cross-section. See Section 3.2.
- 3) The conformal coating of a magnetic material onto a polymeric scaffold via chemical assisted or chemical vapor deposition, such as electroless or atomic layer deposition, respectively, as shown in Figure 5c with a tubular cross-section. See Sections 3.3.1–3.3.2.
- 4) The direct writing of magnetic materials using prefunctionalized resists (predominantly with magnetic nanoparticles) and subsequent polymerization and postprocessing or by the direct photoreduction of the magnetic species into the desired geometry, as shown in Figure 5d with a composite cross-section. See Section 3.4.

It is important to note that each functionalization method yields different geometric implementations of the magnetic material, which in turn affect the possible remanent spin textures, field-dependent magnetization, and switching, as well as possible spin-wave modes. However, these phenomena are not simply dependent upon the geometry (e.g., 3D geometry, roughness) but are also dictated by the intrinsic properties of the deposited material (e.g., magnetocrystalline anisotropy, damping, saturation magnetization) As such, we refer the reader to several studies that provide examples of the rich and diverse magnetization textures^[23,30,42,52,123-128] dynamics,^[32,39,125,129-131] and spinwave behavior^[22,23,40,54,56,68,132,133] that can be realized in specific geometry-material combinations.

bar 50 µm. Reproduced under the terms of the CC-BY 4.0 license. [114] Copyright 2021, The Authors, published by Springer Nature. I) SEM of single lines fabricated via few-photon irradiated TPL. Scale bar 100 nm. Reproduced under the terms of the CC-BY 4.0 license. [115] Copyright 2025, The Authors, published by Springer Nature. m) SEM of an octahedral truss lattice fabricated via digital holography TPL using 64 foci and n) 400 foci. Scale bars 50 µm. Reproduced under the terms of the CC-BY 4.0 license. [117] Copyright 2023, The Authors, Springer Nature.



Table 2. Comparison of available magnetic materials, equipment costs, deposition conditions, deposited geometry, and resolution/feature size limitations for various deposition schemes. Substrate temperature T_{so}, deposition environment pressure P_d.

Deposition scheme	Materials	Equipment cost [\$]	Deposition conditions	Deposited geometry	Feature size or resolution limited?
Thermal evaporation	 Limited to relatively low melting point materials High purity 3D transition metals and alloys^[134,135] M_s can be optimized to near bulk values. 	≈20k	 Nanometer-scale control of deposit thickness Controllable deposition rate T_{su} ≈ 500 K, uncontrolled T_{so} ≈ 1.2×10³ K (for Ni, Fe, Co) P_d < 10⁻⁵ mbarl¹³6] Substrate independent (dependent upon appropriate lattice matching) 	 Non-conformal and shadowing Substrate coated^[137] Open-shell^[138] 	Feature size
Sputtering	 Effectively no limit on materials available High purity 3D transition metals and alloys; soft and hard magnetic alloys, magnetic oxides, complex stoichiometries[135,139] M_s can be optimized to near bulk values 	≈200k	 Nanometer-scale control of deposit thickness Controllable deposition rate T_{ss} ≈ 500 K, controllable T_{so} < 700 K P_d < 10⁻³ mbar⁽¹³⁶⁾ Substrate independent (dependent upon appropriate lattice matching) 	Non-conformal ^[38] with shadowing, or conformal ^[140] using rotation Substrate coated Open-shell ^[61] and tubular ^[140]	Feature size
Electrodeposition	Wide range of available magnetic metallic complexes High purity 3D transition metals and alloys; soft and hard magnetic alloys, magnetic oxides, complex stoichiometries[141,142] Ms can be optimized to near bulk values	≈ Sk	• Nanometer-scale control of deposit thickness • Controllable deposition rate • $T_{av} \approx 400 \text{ K}$, uncontrolled • $T_{co} < 400 \text{ K}$ • Ambient P_d • pH dependent • Conductive substrate	 Conformal Solid Template removal required[145,144] 	Resolution and dark erosion (for positive-tone resists) ^[143]
Electroless deposition	 Limited by available metallic complexes, reducing and functionalization agents Composite magnetic materials (cobalt, nickel, iron, alloys^[145–147], magnetic oxides^[148]) with a reducing agent M_s up to 50% lower than bulk^[149] 	₹	• Limited control of deposit thickness due to autocatalytic reactions • Poorly controlled deposition rate • $T_{so} < 400 \text{ K}$ • Ambient P_{d} • pH dependent • Substrate independent	Conformal Tubular ⁽¹⁴⁸⁾ Substrate coated	Feature size
Atomic layer deposition	 Limited by precursor gases High purity 3d transition metals and alloys, binary/temary/quartemary iron oxides^[150] M_s can be optimized to near bulk values^[65] 	≈500k	• Atomic-scale control of the deposit • Low deposition rate • $T_{ac} < 600$ K, controlled • $T_{co} \approx 500$ K • $P_{d} \approx 10^{-5}$ mbar • Substrate independent	Conforma ^[64] Tubular Substrate coated	Feature size
Direct writing	 Limited by compatibility between nanoparticles/metallic acrylates and resists/hydrogels Low purity superparamagnetic iron oxides Fe₂O₃, Fe₃O₄, and ferromagnetic Ni acrylates^[7/81,151] M_s up to 50% lower than constituent nanoparticles^[152] 	수	 Reduced control over deposit thickness/concentration Deposition rate limited by printing rate Ambient T_{su} and T_{so} Ambient P_d Resist dependent Substrate independent 	 Embedded material in polymer geometry Organic/magnetic composite[77,81,151] 	Feature size



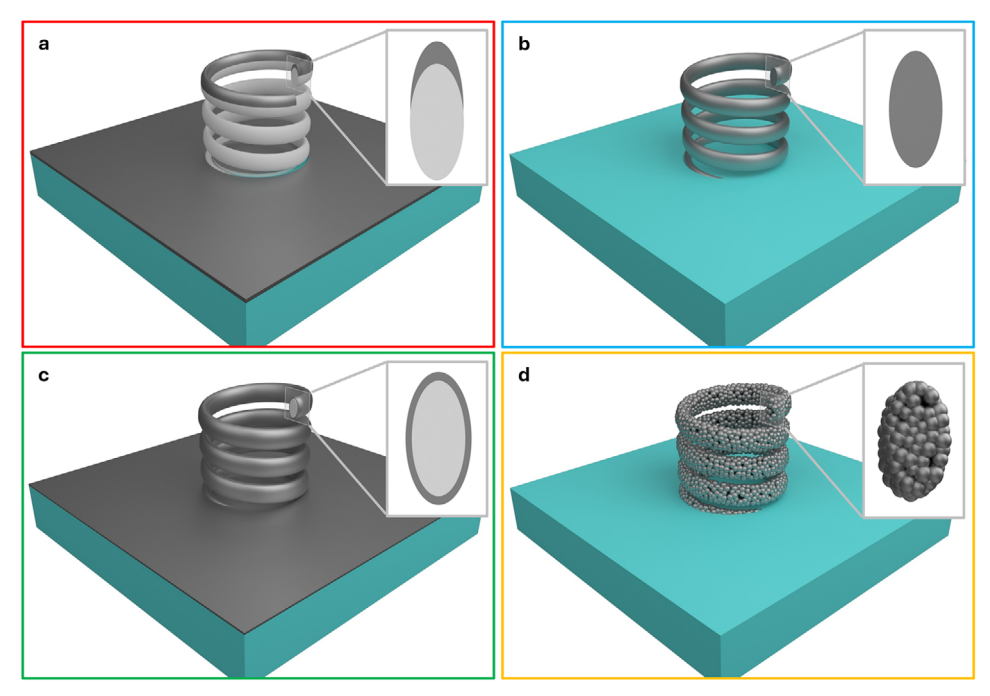


Figure 5. Magnetic material depositions. a) Open-shell structures via physical vapor depositions such as thermal evaporation or sputtering. b) Solid structures via template-assisted electrodeposition. c) Conformal tubular coatings via electroless deposition or atomic layer deposition. d) Direct writing of magnetic structures using functionalized resists.

3.1. Open-Shell Geometries via Line-of-Sight Depositions

Physical vapor deposition (PVD) is a class of well-established techniques for depositing highly pure films, with a wealth of literature exploring the processes. [122,153–155] Whilst electron-beam evaporation has been demonstrated for realizing bio-compatible magnetically actuated microrobots, [156,157] the main PVD techniques used in the metallization of 3D nanostructures fabricated using TPL, and form the main subject of this section, are DC magnetron sputtering [60] and thermal evaporation. [48]

Both approaches yield line-of-sight (LOS) deposition: metallization occurs for any point on the sample with a direct line of sight to the source, with key implications for the resultant nanostructures. Applied to a 1D single-voxel wide nanostructure, these processes yield crescent-shaped cross-sections[138,158] with curvature previously shown to introduce additional energy terms^[52,132] and a non-uniform thickness yielding a non-trivial demagnetizing factor. In addition, inhomogeneous growth-induced anisotropy can occur depending on the surface normal inclination with respect to the LOS. This complexity presents challenges but also an interesting opportunity in, e.g., magnonics, allowing for localization of spin-waves, [50] particularly at the thinner edges, [54] opening potential for magnetic sensing and information transmission devices without Joule-Lenz heat emission.[159-161] Combining TPL with LOS sputtering also has significant applications in micro-robotics and has also been demonstrated as a viable 3D cell culture platform, with magnetic actuation achieved via a Ni layer and biocompatibility with a Ti layer.[162]

Key features of LOS depositions are shadowing and the presence of materials upon the substrate, placing constraints on the

design possibilities; the former results in discontinuity of the functional material where structures overlap, and the latter can introduce undesirable interactions with the nanostructure, additional signal during characterization, risking spurious results, and design challenges for electrical measurements where substrate film introduces short-circuits. However, shadowing may also be a useful tool to address limitations associated with the substrate film. Recent work^[58] on chiral domain wall conduits exploited shadowing to produce disconnected regions upon the substrate film and create convenient contacts for electrical measurements (Figure 6a). Notable examples of 3D artificial spin ice (3DASI) lattice fabrication used TPL scaffolds that are several unit cells thick which elucidated a diverse phase diagram with distinct charge crystal and spin ice phases (Figure 6b). Previous studies on such systems using Brillouin light scattering (BLS) revealed a rich magnon spectra for these 3DASI (Figure 6c). The fundamental physics elucidated from these systems arises despite only the top unit cell being exposed during evaporation, where shadowing prevents magnetic material from being cast upon the lower layers, such that the 3DASI structure is disconnected from the substrate with sufficient distance to minimize dipolar interactions. [48,49,163] Despite the effectiveness of this approach in minimizing these unwanted interactions, signal from the substrate film may remain present in optical measurements with distinct features in magnetooptical Kerr effect (MOKE) measurements, indicative of switching in the substrate at low fields.[48]

Low-field switching in the substrate film has, however, proven beneficial. With a sinusoidal nanowire connected to the substrate (Figure 6d–e), domain walls were injected into the wire at low fields to probe local pinning potentials attributed to local



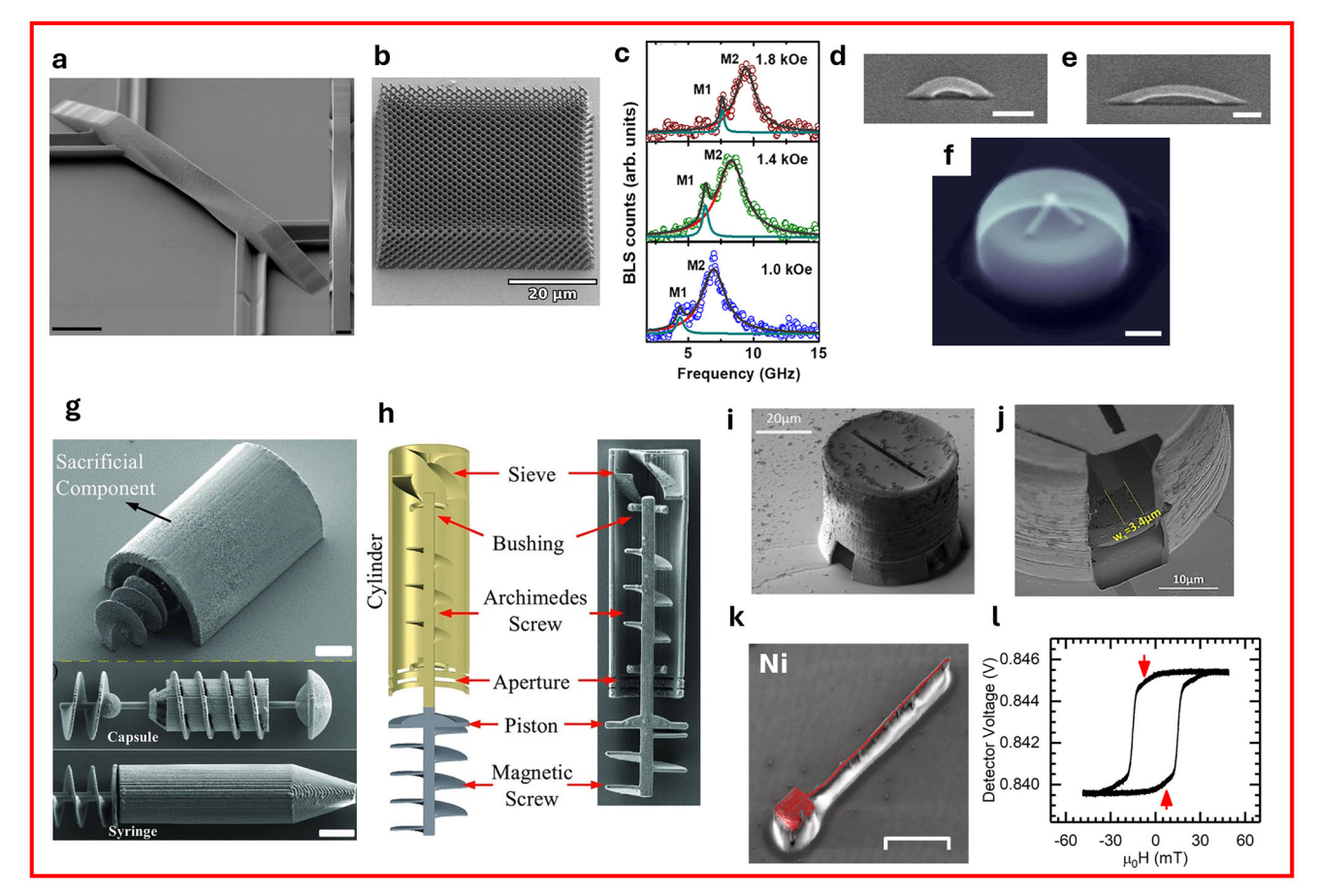


Figure 6. Physical vapor deposition techniques used with TPL nanostructure fabrication. a) Scanning electron microscopy (SEM) of a twisted domain wall conduit, metallized via sputtering, with wire ends connected to the substrate, a v-shaped structure shadows the substrate during deposition creating discrete sections of film to be used for electrical connections. Scale bar 5 µm. Reproduced under the terms of the CC-BY 4.0 license [58] Copyright 2025, The Authors, published by Springer Nature. b) SEM of 4 unit-cell thick 3D artificial spin ice (ASI) lattice metallized via thermal evaporation, where the lower layers are shadowed during evaporation to disconnect the lattice from the substrate. Scale bar 20 µm. Reproduced under the terms of the CC-BY 4.0 license. [51] Copyright 2023, The Authors, published by Springer Nature. c) Brillouin light scattering (BLS) spectra for different applied fields to a diamond lattice 3D ASI. Reproduced under the terms of the CC-BY 4.0 license. [50] Copyright 2021, The Authors, published by American Chemical Society. d-e) SEM images of sub-100 nm width sinusoidal nanowires of different spatial wavelengths, metallized via thermal evaporation. Scale bars 1 µm. Reproduced under the terms of the CC-BY 3.0 license. [131] Copyright 2024, The Authors, published by Royal Society of Chemistry, f) Electronic contrast of a tripod structure imaged using soft X-ray laminography metallized via DC magnetron sputtering with wires connected to a sacrificial base used to enable deformation free pyrolysis. Scale bar 1 µm. Reproduced under the terms of the CC-BY 4.0 license. [61] Copyright 2022, The Authors, published by AIP Publishing, g-h) SEM and schematics of 3D magnetic micromachines consisting of magnetic and non-magnetic components fabricated using a sacrificial mask and thermal evaporation. Scale bars 20 µm. Reproduced with permission. [165] Copyright 2015, Wiley. i) SEM of sacrificial stencil mask with (j) the inside exposed via focused ion beam milling to reveal a thermally evaporated Cr wire. Scale bars (k) 20 μm, (l) 10 μm. Reproduced with permission.[166] Copright 2019, Elsevier. k) EDX map of a magnetic nanowire raised above the substrate, fabricated using a poly-acrylic acid (PAA) sacrificial layer to remove the substrate film. Scale bar 20 μm. Reproduced under the terms of the CC-BY 4.0 license. [168] Copyright 2023, The Authors, published by Cardiff University. I) Hysteresis loop of 3DASI fabricated using a PAA sacrificial layer captured via MOKE magnetometry, showing no clear contribution from substrate film. Reproduced under the terms of the CC-BY 4.0 license. [137] Copyright 2023, The Authors, published by Springer Nature.

roughness and the nanowire cross-section.^[131] Domain wall injection at low fields has also been shown to enable control of more complex structures such as artificial spin ice building blocks (Figure 6f), where the magnetic texture of the film may be exploited to tune the degeneracy of different vertex configurations or control the injection of magnetic charge.^[61]

Despite the success of nanostructure design either minimizing or exploiting the impact of the substrate film, the presence of substrate film limits design choices; the ability to selectively remove deposited materials enables a broader range of accessible geometries and characterization methods. Sacrificial layers to

remove materials from regions where it is undesirable are well-established in 2D device fabrication, with bilayer approaches using a lift-off-resist (LOR) covered with the positive-tone S1813 photoresist, shown to be suitable for 3D nanostructuring with FEBID.^[164] However, the chemical incompatibility often restricts this approach for TPL fabrication due to TPL developer chemicals dissolving the sacrificial layer before deposition can occur.

Selective deposition through PVD on devices written via TPL may be achieved by exploiting shadowing during deposition using sacrificial masks. Huang et al.^[165] reported on the fabrication of complex micromachines for the delivery of therapeutic

payloads, requiring fine control over the movement of some components relative to others via external magnetic fields. Selective deposition was achieved with the sacrificial structure (Figure 6g). that could be mechanically removed with a micromanipulator probe. Using this approach, the authors were able to produce magnetically actuated micro-scale transporters (Figure 6h), capsules with removable caps, and syringes with sliding plungers. Puce et al.[166] extended this approach by patterning the masks to produce sacrificial stencil masks at a smaller scale, where mask removal using micromanipulators may not be feasible. A layer of SU-8 was spin-coated upon the substrate, followed by a drop-cast layer of IP-L, with only the latter being soluble in isopropanol. The structures are written across both resist layers, with the desired structures anchored to the substrate and the sacrificial mask anchored to the SU-8 layer only. An isopropanol alcohol (IPA) bath removes the unexposed IP-L to leave the structures on the SU-8 layer upon which metals are evaporated. The remaining SU-8 layer is subsequently placed in a developer to wash away the stencil mask. Figure 6i shows an SEM of the stencil after metallization, with the stencil mask opened through focused ion beam milling to reveal a well-defined Cr wire inside (Figure 6j). The Cr wire deposition was shown to be slightly off-axis due to parallaxes of the sample and source position. One can envisage a similar approach without the stencil mask; however, a brief flood-exposure of the SU-8 layer is required to prevent diffusion of the resists affecting their optical and chemical characteristics. This flash exposure yields a thin skin on the SU-8/IP-L interface such that an ultrasonic bath is required to remove the substrate film, rendering the procedure infeasible for delicate 3D nanostructures.

A material suitable for a sacrificial layer must remain unaffected by the developers in the TPL process, and chemicals used to perform the lift-off must not affect the polymer scaffolds created using TPL. Although chemically compatible, the SU8 sacrificial layer requires an ultrasonic bath, damaging the 3D nanostructures. In contrast, a LOR/S1813 bilayer process eliminates the need for an ultrasonic bath; the PGMEA developer used to remove unexposed IP-L also removes the S1813. Polyacrylic acid (PAA) was identified as a useful material for sacrificial layers in micromachining owing to good film uniformity after spin-coating, stability upon immersion in conventional development solvents, and solubility in water that remained after photolithography.[167] Although its solubility in water is a desirable feature, the latter also indicates that the material cannot be patterned using standard lithographic methods. One notable feature of PAA is that it can be ablated with relative ease using a TPL system without modification. After spin-coating PAA onto a glass substrate, the sample is mounted into the TPL system, and trenches are ablated into the PAA. A key strength of this approach is that IP-L photoresist may be drop-cast without removing the sample from the sample holder, allowing for precise alignment when writing structures into the ablated trenches. After the standard development process and PVD deposition, the sacrificial layer may be removed in a DI water bath. The outlined approach was used to produce simple domain wall conduits with DW injection pads, [137] with energy dispersive X-ray (EDX) maps at the Ni L3 line showing complete removal of the substrate film (Figure 6k). [168] When applied to the fabrication of 3DASI lattices, signal from substrate film in MOKE measurements was eliminated (Figure 61), enabling deeper investigation into the switching behaviors of 3DASI without risk of spurious features from these contributions.

3.2. Solid Geometries via Template-Assisted Electrodeposition

Template-assisted electrodeposition utilizes a prefabricated porous template, such as ion-etched polymer or anodized alumina oxide (AAO) templates, upon a working electrode. The desired metal is deposited into the pores via electrodeposition, and the deposited metal takes the form of the pore geometry, and finally, the template is removed. The choice of working electrode is a critical consideration in the design of the deposition scheme, affecting the specific reduction potentials, pore filling fractions, as well as the final structural morphology of the deposit. [169] Additionally, the specific deposition scheme (potentiostatic, galvanostatic, pulsed, etc.) is critical in determining the efficiency of deposition, which can be limited by the formation of screening double-layers.

Ion-etched polymer templates, where heavy ions are bombarded upon a polymeric template, effectively damage the area of impact, and following a cleaning procedure to remove the residual polymer, result in a hollow nanoscale pore with a range of symmetric and asymmetric pore geometries.^[170] These templates have been used to realize high aspect ratio Co,[171] Fe,[172] Cu/Ni core-shell, [173] Co/Cu multilayered [174] and Co₈₁Cu₁₉ alloy [175] nanowires. The surrounding templates can be dissolved relatively easily with solvents; however, custom pore geometries require the use of accelerator facilities.^[141] AAO templates are the more cost-effective and scalable alternative^[176] of templates with well-understood etching and anodization schemes, one can engineer high-density pores with diameters ranging from tens to hundreds of nm with micron lengths. There is a significant degree of freedom in the pore geometries using pore etching techniques, allowing the realization of geometric bamboo-like^[177] and continuously varying diameter modulations, [178] compositional modulations, [179-181] as well as realizing 3D interconnected networks of nanowires.^[182] This methodology has paved the way for important studies on domain wall nucleation and motion,[32] chirality-dependent domain wall behavior,[183] experimental observation of Bloch-point domain walls,[31] and the associated transformations under external fields.[39] Again, the templates are relatively easily dissolved to reveal the nanowires, typically by immersion in NaOH, and the nanowires can be extracted via solvent dispersion. However, the major drawback of ion-etched polymer or AAO templates is the inability to arbitrarily design 3D pores. Direct printing of templates with arbitrary pore geometry is then an appealing feature afforded by TPL.

TPL has been combined with electrodeposition extensively by using positive-tone resists, where the designed pattern directly equates to the final geometry of the empty channels, which can then be metallized via electrodeposition. Schürch et al. demonstrated this methodology whereby an Indium-Tin Oxide (ITO) conductive substrate was spin-coated with a positive-tone resist, helical channels defined via TPL, followed by Ni electrodeposition and resist removal via immersion in an ultrasonic bath of acetone.^[184] This work demonstrated arrays of nanocrystalline Ni micro-springs with custom geometries (**Figure 7a**). Pore filling factors were improved by the use of electrodeposition

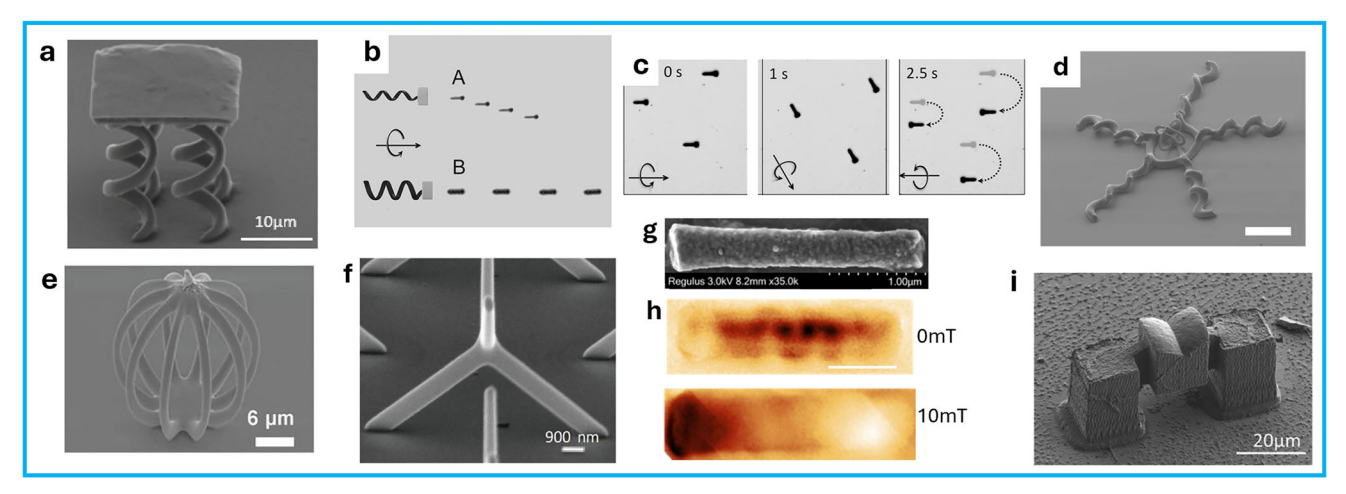


Figure 7. Solid geometries via template-assisted electrodeposition. a) SEM of Ni micro-springs fabricated via positive resist template-assisted electrodeposition. Scale bar 10 μm. Reproduced with permission. [184] Copyright 2020, Elsevier. b—c) Optical images of 20 μm length hybrid CoNi-polypyrrole (head-tail) helical swimmers manipulated by rotating magnetic fields with varying magnitude. c) Swarm-like manipulation at different time intervals. Reproduced with permission. [186] Copyright 2013, Wiley. d) SEM of interlocked Fe and PDMS structure. Scale bar 50 μm. Reproduced under the terms of the CC-BY 4.0 license. [187] Copyright 2020, The Authors, published by Springer Nature. e) SEMs of Fe roller-type microrobots printed via positive resist template-assisted electrodeposition. Scale bar 6 μm. Reproduced with permission. [78] Copyright 2019, Wiley. f) SEM of Co tetrapods fabricated via positive resist template-assisted electrodeposition. Reproduced under the terms of the CC-BY 4.0 license. [143] Copyright 2018, The Authors, published by Springer Nature. g) SEM of a toppled Ni nanowire fabricated with negative resist template-assisted electrodeposition. Scale bars 1 μm. h) Corresponding magnetic force microscopy (MFM) images taken at remanence (top) and under a saturating easy-axis field (bottom). Scale bars 1 μm. Reproduced under the terms of the CC-BY 4.0 license. [144] Copyright 2020, The Authors, published by MDPI. i) SEM of a Ni micro-bridges fabricated via negative resist template-assisted electrodeposition. Scale bar 20 μm. Reproduced with permission. [189] Copyright 2018, Wiley.

simulations to inform the template design, as such voids were designed at the electrolyte-substrate interface. Additional voids at the entrance of the pore were fabricated to allow transfer of the micro-springs from the original substrate for further mechanical characterization, showing that such structures were able to undergo repeated stress loads, and critically that this methodology can tailor design micro-mechanical systems.

Another promising application of TPL template-assisted electrodeposition is in magnetically driven micro-robotics, specifically in the context of in vivo targeted drug delivery, and in vitro transport of microstructures, [77,185] where TPL offers the versatility in terms of the design and electrodeposition in terms of the range of magnetic and biocompatible materials. Bi-component magnetic and polymeric helical micro-robots, consisting of a CoNi head for magnetic actuation, and an intrinsically conductive polymer tail for propulsion in liquid environments, have been demonstrated by Zeeshan et al.[186] Helical channels and a void at the electrolyte-substrate interface were fabricated within a positive resist using TPL, followed by a two-step electrodeposition of the magnetic-polymer parts, and finally release of the robots by removal of the surrounding template. Example optical timelapse images in Figure 7b, taken at 1.25 s intervals, showcase the differences in motion of two such structures with different helical radii, under a rotating external magnetic field. The geometry and rotational frequency of the field allows precise control over the velocity and propulsion regime, with swarms of microrobots shown to be controlled in unison as the rotational axis is rotated through 180° in Figure 7c.

Multi-material and multi-functional micro-robots consisting of interlocked Fe and polymer structures have been shown by Alcântara et al. [187] in which a positive resist was used to pattern

both the metallic and polymer components using electrically connected and isolated channels, respectively, with an example Fe-PDMS interlocked structure shown in Figure 7d. Such structures were shown to exhibit complex motion under rotating magnetic fields in liquid environments with multiple locomotion strategies afforded by the coupled design of the soft and hard components. Purely iron microrobots, with an example angled SEM of a rollertype microrobot shown in Figure 7e, with excellent biocompatibility, have been demonstrated by Alcântara et al. [78] Here, the authors overcome the typical depth of field limitations and requirements for a transparent substrate associated with immersionconfiguration printing by using dip-in writing. This allowed thick layers of resist to be spin-coated, and channels of up to 400 µm to be realized, and the pores were designed with equal segmented path lengths and included multiple outlets at the resist-electrolyte interface and contact points at the electrolyte-substrate interface to minimize plating issues and development time.

This methodology has also been demonstrated to realize complex 3D Co nanostructures as shown by Williams et al., [143] with minimum lateral feature sizes on the order of 430 nm and low surface roughness, with an example free-standing Co tetrapod shown in Figure 7f. Dark erosion of the exposed channels in this work was shown to be a significant detriment to the minimum features achievable, resulting in structures firmly within complex multi-domain magnetization patterns as characterized using spin-polarized SEM. This work demonstrated a first step toward using this methodology for magnetic nanostructure fabrication, and such structures were further characterized by Sahoo et al. [75] using time-resolved magneto-optic Kerr effect microscopy, revealing three spin-wave modes at 1, 10, and 30 GHz.



www.afm-journal.de

A method of circumventing such dark erosion effects on minimum features is using a negative resist, where the minimum pore size is determined by the lateral (for purely vertical pores) and axial resolution (for angled or lateral pores) as given by Equations (1) and (2). Instead of directly patterning the desired structure into the pores, one polymerizes the entire template except for the desired pore geometry. This methodology warrants the use of pre-patterned electrodes or by using a protective non-conductive layer upon the conductive substrate to avoid unwanted electrodeposition and necessitates the use of harsher template removal strategies, such as high-powered plasma ashing with various gases. Askey et al.[144] demonstrated this negative resist TPL template-assisted electrodeposition for the realization of cylindrical Ni nanowires (Figure 7g), with a measured average feature of 420 nm and a length of 2.82 µm. Magnetic force microscopy of such systems revealed a complex multi-domain pattern at remanence (Figure 7h top), with an alternating bright-dark contrast throughout the nanowire akin to those of spiraling domains found in cylindrical nanowires with compositional and diameter variations. [181,188] Further optimization of such templates has been shown to realize cylindrical nanowires with diameters below 200 nm, which is on the order of the resolution limit for $\lambda = 780$ nm and NA = 1.4. Negative resist TPL templates have been used to realize Ni microbridge architectures using reverse pulse electrodeposition, where the design and deposition pulse parameters were optimized by electrodeposition simulations as shown by Schürch et al.[189] Microbridges were chosen due to their geometrically challenging aspects in terms of electrodeposition (geometric bottlenecks, diffusion, and growth), and to allow for direct mechanical testing of such complex 3D architectures. Arrays of bridges were successfully fabricated (Figure 7i), using this methodology with homogenous nanocrystalline and cavityfree structures with high shape fidelity with respect to the original designs.

3.3. Tubular Geometries via Conformal Coatings

3.3.1. Electroless Deposition

One of the main challenges of transforming TPL scaffolds into magnetic nanostructures is the fact that typical conformal deposition techniques, such as atomic layer deposition and electrodeposition, often require high temperature processes or require the scaffold to be conductive, while vacuum metallization techniques, such as sputtering or thermal evaporation, often struggle to cover 3D geometries uniformly, especially due to shadowing effects. For the polymer scaffold, which is better suited to low temperature post-processing to maintain the form of the scaffold (particularly important for high resolution scaffolds), and which is insulating, achieving conformal coating of magnetic materials can therefore be challenging.

A promising alternative growth technique for the conformal coating of 3D polymer nanoscaffolds comes with electroless deposition (ELD), which enables the growth of materials onto complex geometries without the need for electrical current/conductive substrates or high temperatures, Table 2. ELD is particularly relevant for the deposition of materials on polymer substrates^[190] and is well established for the de-

position of Ni, Cu, Ag, Au, and related alloys, with a number of existing industrial applications such as electromagnetic shielding, printed circuits, and in recording media. [145,191] This ability to conformally coat non-conductive substrates with Ni offers a promising opportunity for the field of 3D nanomagnetism.

In the ELD process, the whole sample is immersed in a reactive chemical bath, allowing for the uniform deposition of a metal layer on the entire surface, regardless of geometry or substrate conductivity. The principle behind electroless deposition is based on a redox chemical reaction that occurs when a substrate is placed in a solution containing metal ions and a chemical reducing agent.[146,147,192] When the reducing agent is oxidized, electrons are donated to metal cations in the solution, which are reduced and deposited as a film on the activated surface. The chemical bath typically contains several components:[146,147,192] metal salts, a reducing agent, complexing agents to stabilize metal ions, pH buffers, and a variety of additives that influence deposition rate, grain structure, surface morphology, or film thickness. Once nucleation begins on the surface, metal deposition proceeds autocatalytically. As the process is performed at relatively low temperatures, typically below 100 °C, the technique is particularly compatible with heat-sensitive substrates/polymers. It also provides good conformality even in deep or narrow features, allowing for the deposition in high aspect ratio templates for the fabrication of, for example, nanowires and nanotubes.[130,193] Furthermore. ELD requires simple equipment and is scalable for batch processing, offering a low-cost and accessible route to functional device fabrication. However, several challenges are associated with ELD. The stability and composition of the plating bath are critical: small variations in temperature, pH, or concentrations can lead to inconsistent deposition or layers with a high number of impurities. Furthermore, the initial surface activation step, necessary for initiating the redox reaction, is critical to produce uniform coatings with good adhesion. Moreover, because the process is autocatalytic, internal stresses may build up in the deposited films, leading to cracking or delamination, particularly on flexible substrates.

While there have been a number of demonstrations of electroless deposition for larger systems, there have recently been a few works harnessing electroless deposition for the realization of magnetic nanowires and nanotubes.[130,193-195] In particular, magnetic nanowires have been realized by self-assembly of nanoparticles through electroless deposition under magnetic fields.[194,195] Electroless deposition has also been used to realize straight magnetic nanotubes of diameter 300 nm through the conformal deposition in polycarbonate membranes.^[130] The nanotubes were shown to exhibit an azimuthal magnetic domain configuration, which was then characterized with electrical transport measurements.[130,193] For the realization of 3D nanostructures, the combination of electroless deposition with TPL represents a promising direction, with several demonstrations of electroless plating of a variety of metals upon TPL-fabricated scaffolds.[196-198] To the best of our knowledge, the first demonstration of electroless deposition of a magnetic layer on TPLfabricated polymer lattice was shown by Mieszala et al.,[199] where TPL was used to print a range of microcellular architectures and then coated with < 100 nm of amorphous Ni₇₈B₂₂ as determined by X-ray diffraction, demonstrating conformal coverage of the

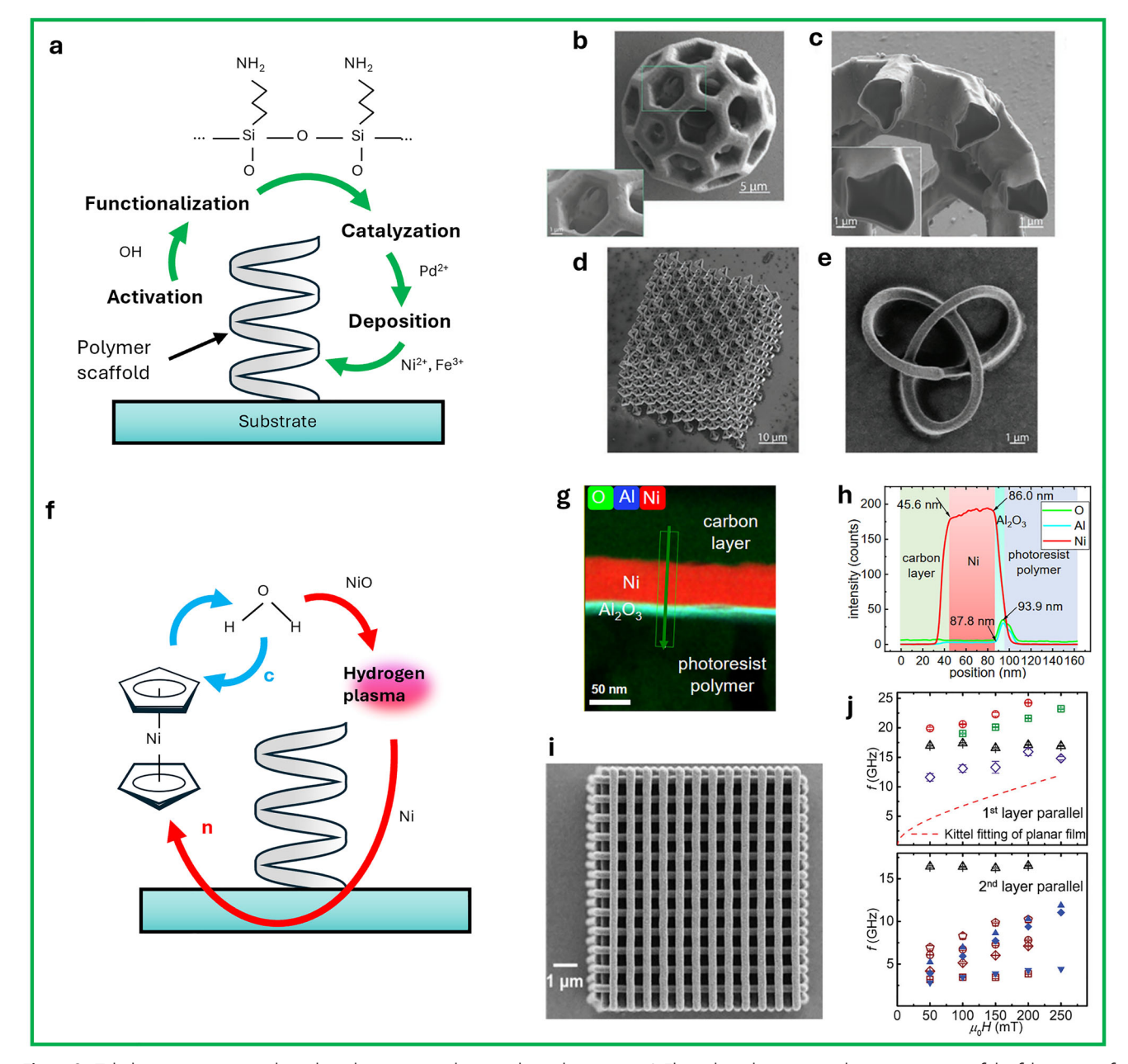


Figure 8. Tubular geometries via electroless deposition and atomic layer deposition. a) Electroless deposition scheme consisting of the fabrication of the two-photon lithography scaffold, activation of the surface, functionalization, catalyzation and electroless deposition. b) 3D polymer nanostructures with a magnetic Ni-Fe(B) layer: buckyball structure (b) and (c), Artificial pyrochlore lattice (d) and trefoil-knot (e). b–e) Reproduced with permission. Copyright 2020, Wiley. f) Schematic of atomic layer deposition (ALD), with c pulses of nickolecene and water molecules to produce a monolayer of NiO, followed by n pulses of hydrogen plasma to reduce NiO to Ni. g) Transmission electron microscopy (TEM) image of ALD coated polymer, with green line profile shown in (h) illustrating the compositional variations. g) Scale bar 50 nm. i) SEM image of a woodpile. Scale bar 1 μm. j) BLS spectra for a woodpile under an externally applied magnetic field, showing up to 25 GHz resonances. g–j) Reproduced under the terms of the CC-BY 4.0 license. [64] Copyright 2023, The Authors, published by Wiley.

polymer structures. However, only the mechanical properties of the lattices were characterized. NiFeB layers were deposited via electroless deposition on TPL-fabricated scaffolds by Pip et al., [149] with schematic of the activation, functionalization, catalyzation and deposition steps on a polymer scaffold shown in **Figure 8a**. Specifically, it was shown that the magnetic properties of the NiFeB could be maintained when deposited on a polymer sub-

strate fabricated with TPL. Moreover, a robust, conformal coating was demonstrated on a variety of complex 3D microstructures, including a buckyball, a woodpile lattice structure, and a topologically non-trivial trefoil knot (Figure 8b–e). Bernasconi et al.^[200] further demonstrated a CoNiP magnetic coating via electroless deposition upon TPL-fabricated micro-helices, which were actuated via rotating magnetic fields, further highlighting the range



www.afm-journal.de

of potential magnetic materials to be deposited using this metallization route.

In summary, electroless deposition is a versatile method for coating complex 3D TPL structures with magnetic materials. By enabling uniform coating of magnetic materials on nonconductive and high-aspect-ratio or complex geometries, ELD expands the functionality of 3D-printed nanostructures, paving the way for advanced applications in nanomagnetism, soft robotics, and next-generation microsystems.

3.3.2. Atomic Layer Deposition

Atomic layer deposition (ALD) has enabled 3D devices in microelectronics, such as deep-trench capacitors and field-effect transistors in which a gate electrode wraps around a vertical semiconductor channel. [201] ALD is a shadow-free deposition technology on the wafer scale, which offers uniform conformal coatings and thickness control down to the monoatomic layer. At the same time, substrate temperatures can be low (<500 K). These are key advantages that make ALD a standard technology in microelectronics and enable the very large-scale integration in multi-level device architectures. However, ALD-grown magnetic layers are not yet an industry standard.

Many of the magnetic materials used in spintronics applications so far consist of transition metals like Co, Fe, and Ni. ALD for such metals is, however, particularly challenging compared to the many oxidic compounds for which optimized ALD processes are available in production tools. The status of ALD processes for, e.g., ferrimagnetic oxides and other magnetic compounds is summarized in.[150] Though one finds a considerable number of reported ALD processes for various magnetic materials, not all of them include the characterization of relevant magnetic properties, such as those mentioned above (in the introduction). Still, there have been some specific breakthroughs that substantiate the potential of ALD for a scalable 3D magnetic device technology. A detailed review of ALD of magnetic thin films has been published recently by T. Jussila et al.[150] In this excellent review, the authors have critically discussed the status concerning almost 40 different magnetic materials. However, they have not yet considered the recently performed combination of an ALD-grown ferromagnetic element and a TPL-created nanotemplate, which we discuss in the following.

There have been several attempts to create functional layers containing Co, Ni, or Fe by either thermal or plasma-enhanced ALD with and without post-annealing in a reducing atmosphere of hydrogen. Following,^[150] the in situ combination of these different materials synthesis strategies has so far led to the currently best quality of an ALD-grown ferromagnetic transition metals.^[66,67] Conformal layers of high-quality Ni were achieved first on vertically standing semiconductor nanowires^[67] and then applied also to TPL-produced nanotemplates.^[64]

First, a pulse of the metal-organic precursor molecule nickelocene (NiCp₂) was applied to the nanotemplate, which was followed by a pulse of water molecules after a purging step using an inert gas flow. The sequentially offered precursor molecules created a thin conformal layer of NiO via thermal ALD at 175 °C, followed by a subsequent purging step. After repeating this thermal ALD process for c times, an intermediate reduction process

was initiated by means of a hydrogen plasma (Figure 8f). This in situ combination of thermal ALD and plasma-enhanced reduction was repeated n times to realize the target thicknesses of the conformal Ni coating, typically between 10 and 30 nm. A final post-annealing is performed at 350 °C in a hydrogen-containing inert gas atmosphere for a few hours. All these temperatures are below the thermal budget for the back-end-of-line processes in microelectronics and the pyrolysis of the TPL resist.^[202] They are also low enough to avoid dewetting. The deposited Ni films with c = 7 and a thickness of 30 nm showed the following properties: a specific resistivity of 8 $\mu\Omega$ cm at room temperature, a saturation magnetization $\mu_0 M_s = 0.5$ T, a relative anisotropic magnetoresistance (AMR) effect of 3.9 % and a small damping parameter $\alpha = 0.025$ which was lower than reported for Ni thin films grown on planar Si(1 0 0) substrates by electron beam evaporation in an ultra high vacuum chamber at a base pressure of ≈ 5 x 10^{-10} mbar.^[65] The coercive field $\mu_0 H_c$ was estimated to be ≈ 5 mT and hence close to 1.2 mT, defining the upper limit of coercive fields for a technical soft magnet. The small coercive field was consistent with the polycrystalline nature of the ALD-grown Ni. The resulting Ni films were smooth and did not have voids. A separate ALD growth study using a similar deposition strategy confirmed the good structural quality of Ni, the uniformity, and the low level of carbon contamination without reporting on the magnetic properties, however.[203]

The ALD process developed in [67] started by intentionally growing first a thin (under)layer of Al₂O₃. Al₂O₃ is among the best studied ALD processes and applicable to many substrate materials. The Al₂O₃ process was already applied to complex polymeric nanotemplates created by TPL when the authors Meza et al.[204] aimed at a mechanical metamaterial. Consistent with a speculation provided in, [203] the Al₂O₃ underlayer allowed H. Guo et al.[64] to transfer the previously developed Ni process (Figure 8f), to free-form polymeric nanotemplates without compromises in conformality and uniformity (Figure 8g-h). Figure 8i shows conformal Ni shells deposited by plasma-enhanced ALD on a several um high 3D woodpile structure created by a TPL process. When applying inelastic light scattering, the low damping of the ALD-grown Ni allowed for the observation of a manifold of collective spin excitations (magnons) in 3D ferromagnetic woodpile structures (Figure 8j).

To enable further progress in functional 3D magnonics and spintronics, the ALD growth of ferromagnetic transition metals Fe and Co is important. Combining pulses of the precursor molecule iron (III) tert-butoxide (Fe₂(OtBu)₆) with nickelocene pulses in a so-called super-cycle ALD process, [150] Permalloy $(Ni_{80}Fe_{20})$ with $\mu_0 M_c = 1$ T was achieved on 3D topographies. [66] Planar films exhibited a large AMR effect (5.6 %) at room temperature. This value indicated appreciable spin-dependent scattering of electrons, qualifying for sensing applications. The minimum coercive field amounted to 3.6 mT, which was more than an order of magnitude smaller than for previously published material. The damping value of $\alpha = 0.013$ was improved compared to Ni and enabled the experimental exploration of magnons controlled by magneto-chiral effects in 3D nanotubes.^[36] Again, Al₂O₃ was used as an underlayer such that free-form 3D Permalloy devices for spintronics and magnonics are within reach.

Reports about the magnetic properties of ALD-grown Co are scarce, but the recently observed spin-dependent tunneling



www.afm-journal.de

of electrons into a planar Co thin film produced by ALD is encouraging. [205] The ALD-grown Co shows a coercive field of ≈130 mT qualifying for a hard magnetic material. The recent developments in ALD growth of ferromagnetic 3d transition metals, hence promise both to upscale fundamental research in 3D nanomagnetism and to enable functional 3D spintronics and magnonics devices based on both soft and hard magnetic materials.

3.4. Direct Writing of Magnetic Materials

So far, this review has covered work that leverages additional deposition techniques to realize magnetic functionality in the printed device. Despite the clear advantages (see Table 2) offered by these techniques, these are coupled with multi-step and sometimes complex and expensive post-fabrication processing to enable magnetic functionality. An extremely attractive prospect is the ability to directly print a magnetic structure with little to no additional post-fabrication deposition or processing to achieve the desired functionality, akin to FEBID, which has paved the way for important work in realizing almost arbitrary 3D ferromagnetic nanostructures. [10,206]

Direct writing of magnetic micro- and nanostructures via TPL is often achieved by the functionalization of a negative resist or a hydrogel with magnetic nanoparticles or a magnetic metal containing species, as shown schematically in Figure 9a. TPL then results in an organic/metallic hybrid composite with the magnetic species embedded within a cross-linked monomer network. This technique has been used extensively in the realization of magnetic microrobotics with several important reviews that detail important recent work in this field. $^{[77,80,81,207-211]}$ By leveraging the freedom of 3D design with the underlying attractive properties of commercially available and custom resists, a range of functionalities can be realized. Typical acrylate-based resists exhibit minimal thermal degradation up to ≈600 K,[202] indicating excellent stability across all biologically relevant temperature ranges. Furthermore, the long-term mechanical stability of commercial resists has been characterized by Koch et al.,[86] showing negligible degradation in flexural properties over time. Polymers with large Young's Moduli on the order of GPa (e.g., IESL-FORTH SZ2080;[212] Nanoscribe IP-L and IP-Dip;[213] and UpNano resists^[214]) allow for rigid actuation of structures under external stimuli, e.g., microswimmers and micromechanical systems. Polymers such as hydrogels with water absorbing capabilities which emulate extracellular matrices, [211,215] and low Young's Moduli typically on the order of MPa (Nanoscribe IP-PDMS resist;^[213] and BIO INX hydrogels^[214]) and even as low as a few 100 kPa for custom hydrogel formulations, [216,217] allow for elastic deformation and actuation under external stimuli, e.g., for applications in biocompatible cell- and soft-robotics.

This methodology allows for the realization of a range of biocompatible 3D microstructures, particularly due to the attractive magnetic actuation aspect of microrobotics, and for the vast array of biocompatible surface functionalizations possible through the metallic-organic composite structure. Superparamagnetic iron oxide Fe₃O₄ nanoparticles are a common choice of magnetic species in resists, with demonstrations of SU-8/Fe₃O₄ composite twist-type actuators by Peters et al. [219] (Figure 9b). Particle

alignment by an external magnetic field during the film softbake enables shape-independent magnetic properties, and such actuators have also been surface-functionalized for increased biocompatibility. Helical-type microrobots have been demonstrated in a range of resist/nanoparticle composites with tunable corkscrew motion in SU-8/Fe₃O₄^[220] and high liquid velocity biocompatible PETA/FePt.[221] Ormocore resist has been combined with superparamagnetic maghemite structure nanoparticles Fe₂O₃ for the realization of polymer/metallic composite scaffolds (Figure 9c), for enhanced osteoblast cell attachment and mineralization under external fields as demonstrated by Paun et al.[152] Micro-gear pairs comprised of an acrylate/Fe₃O₄ composite have been fabricated with no post-fabrication treatments by Peng et al.^[222] (Figure 9d). The authors demonstrated magnetic and non-magnetic micro-gear compatibility with a range of possible transmission ratios, controllable motion via external magnetic fields, dispensing of particles to target locations, and conversion of continuous to discrete motion. Micro-tubes fabricated via single exposure using an optical vortex focal volume have been demonstrated in SZ2080/Fe₃O₄ by Yang et al., [223] shown to be manipulable via rotating fields (Figure 9e), which has allowed for the precise pick-up and delivery of SiO2 microparticles in a liquid environment. Aside from biofunctional microrobots, 3D polymeric/metallic composites are extremely appealing for magnetically actuated micromechanical systems, which are uniquely positioned to offer novel solutions in micro-scale manufacturing.[81] In work by Xia et al.[224] Fe₃O₄ nanoparticles have been surface functionalized to imbue dispersible and photopolymerizable functionalities, to assist in the TPL step, and subsequently dispersed in an acrylate-based negative resist. TPL was then used to define an array of micromechanical structures ranging from magnetically actuated helices and collar-joint micro-turbines in acetone (Figure 9f). Hydrogel/Fe₃O₄ composites have been shown by Geid et al.[216] to act as surface-activated biocompatible cell adhesion promoters which can be manipulated via external magnetic field gradients, effectively stimulating cell morphogenesis (Figure 9g-h). Similar hydrogel/nanoparticle composite materials have been used as biocompatible photothermally deformable 3D structures, with millisecond response times to the incident light, which can undergo multiple repeated deformations without structural degradation, as shown by Zheng et al.[225] (Figure 9i,j).

Whilst nanoparticle and resist composites have been used extensively in fabricating a range of microstructures for biocompatible and mechanical applications, there are significant drawbacks to this methodology. Most importantly, the composite is an impure metallic/organic matrix, where the magnetic proportion typically comprises less than 10% of the relative weight of the structure. Magnetic nanoparticles inherently change the physical and chemical properties of the resist, typically limiting the dynamic range of exposure parameters, as well as the range of available feature sizes and resolutions, and effectively inhibit polymerization due to the often-times high absorption within the nanoparticles on laser exposure.^[81] So, to increase the proportion of the magnetic component in the final structure, one would need to increase the proportion of the magnetic nanoparticles, which in turn further affects the dynamic range for polymerization. Alternative routes to incorporating magnetic (and many other metallic and functional) species into a resist are thus an active

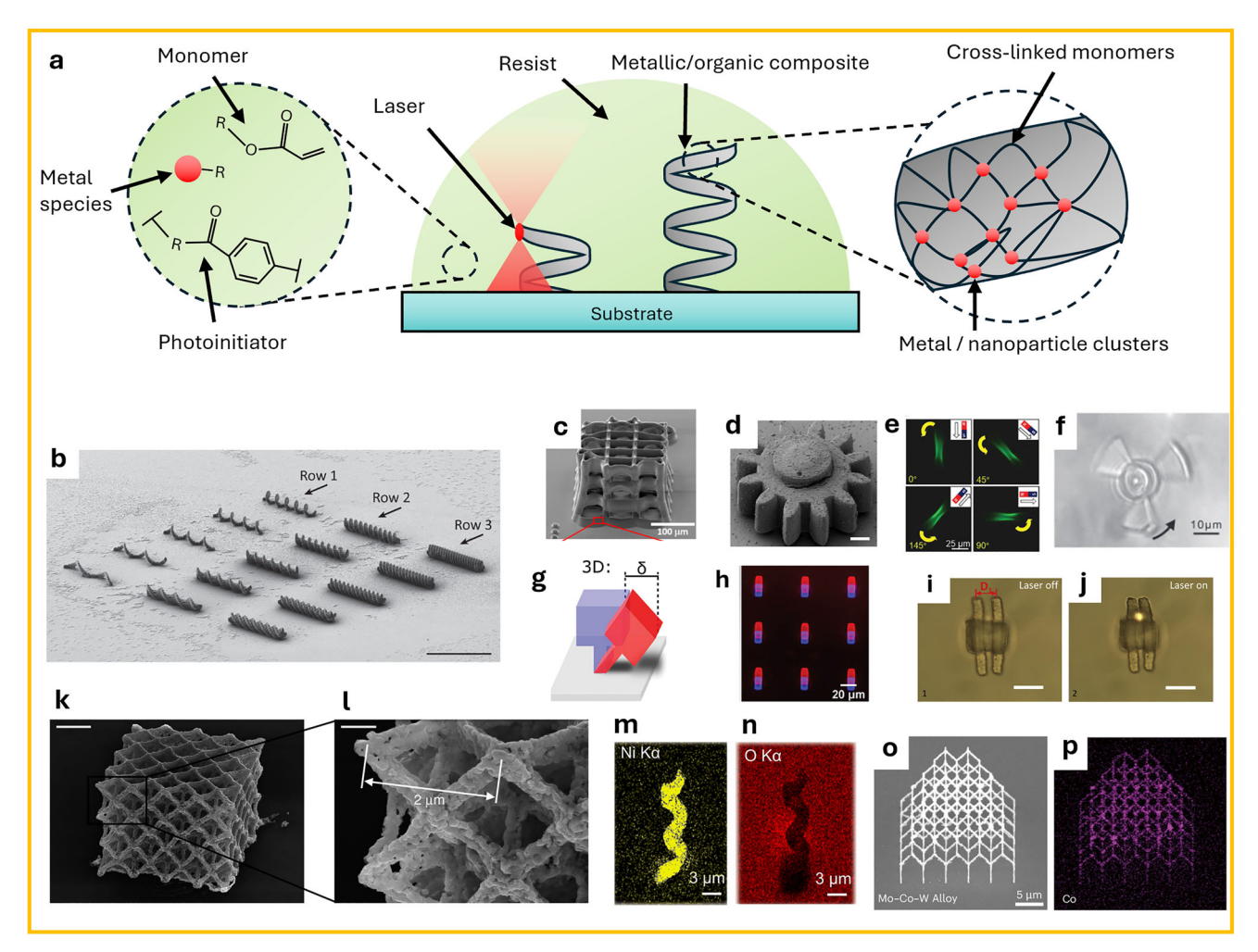


Figure 9. Direct writing of magnetic materials via TPL. a) Simplified TPL process in a functionalized resist consisting of a monomer, photoinitiator and a metallic species (e.g., nanoparticles, metal containing acrylates), left zoomed inset. The final printed structure is a helix consisting of metallic clusters embedded within a cross-linked monomer matrix, right zoomed inset. b) SEMs of magnetic helical microrobots with varying actuator geometries, consisting of an SU-8 and superparamagnetic magnetite Fe₃O₄ nanoparticle composite. Scale bar 50 µm. Reproduced with permission.^[219] Copyright 2014, Wiley. c) SEM of superparamagnetic cell scaffold consisting of Ormocore and maghemite γ -Fe $_2$ O $_3$ nanoparticles. Scale bar 100 μ m. Reproduced under the terms of the CC-BY license^[152] Copyright 2019. The Authors, published by MDPI. d) SEM of micro-gears comprised of polymer and Fe₂O₄ nanoparticle composite. Scale bars 5um. Reproduced with permission.^[222] Copyright 2024, Wiley. e) Fluorescence microscopy images of SZ2080/Fe₃O₄ composite micro-tubes manipulated by an external magnetic field. Scale bars 25 µm. Reproduced with permission. [223] Copyright 2019, Wiley. f) Optical images of an acrylate-Fe₃O₄ composite collar-joint micro-turbine actuated via magnetic field. Scale bars 10 μm. Reproduced with permission. [224] Copyright 2010, Wiley. g) Schematic of the deflection of a magnetic-polymer composite hammer-like 3D structure, h) overlaid optical images of the deflected (red) and undeflected (blue) structures. Scale bar is 20 µm. Reproduced under the terms of the CC-BY license. [216] Copyright 2024, The Authors, published by Wiley. i) Optical image of a hydrogel-Fe₃O₄ composite under no laser illumination, j) with laser illumination illustrating light-actuation. Scale bars 10 µm. Reproduced with permission. [225] Copyright 2020, Elsevier. k–l) SEMs of a Ni nanolattice following pyrolysis. Scale bars 2 µm and 500 nm, respectively. Reproduced under the terms of the CC-BY license. [151] Copyright 2018, The Authors, published by Springer Nature. m-n) Ni and O energy dispersive spectroscopy (EDS) maps in a pyrolyzed Ni magnetically actuated microrobot. Scale bars 3 μm. Reproduced with permission [226] Copyright 2024, Royal Society of Chemistry. o-p) SEM and EDS Co mapping of a direct written alloy via two-photon decomposition. Scale bar 5 µm. Reproduced with permission.[227] Copyright 2024, Springer Nature.

area of research. Instead of mixing magnetic nanoparticles, Vyatskikh et al.^[151] showed that incorporating a Ni containing acrylate with a conventional resist (containing typical cross-linking monomers, photoinitiators) allows for the fabrication of complex micro-architectures, as shown in Figure 9k, and in a post-processing pyrolysis step the organic components are effectively removed, leaving only a nanocrystalline (on order of 21 nm) 3D Ni lattice (Figure 9l), with minimum features of 100 nm with sin-

gle lines. Similar methodology with a Ni-acrylate based resist and post-fabrication sintering has been used in work by Li et al., who fabricated Ni micro-helices with high purity (Figure 9m–n), with various geometric parameters which allowed for the precise manipulation in fast-flowing fluid environments, and demonstrated impressive cargo-carrying capabilities with the ability to move objects 200× the mass of the fabricated helix. Recent work by Wang et al. demonstrated the direct writing of nanoscale



www.afm-journal.de

metals and alloys via two-photon decomposition and optical trapping using a direct laser writing TPL system. Critically, this work forgoes the use of any polymer resists and instead leverages metal precursors both in pure and oxide forms and demonstrates a range of magnetic materials and alloys in complex 3D architectures (Figure 90,p). This work marks a significant step toward optical-based direct writing of arbitrary magnetic materials on the nanoscale.

4. Post-Processing

For the field of 3D nanomagnetism, the ability to fabricate complex 3D geometries with nanoscale resolution – with feature sizes below 100 nm - is key. TPL is a powerful technique for fabricating 3D geometries with submicron resolution - typically on the order of 200 nm for commercial systems. However, as discussed in Section 2.2.1, achieving feature sizes below 100 nm typically requires advances in the process, such as the use of smaller wavelength lasers[90,92,131] and the careful design of photoresists. An alternative route to achieving smaller length-scales comes with the implementation of post-processing steps, to enhance the spatial resolution of larger scaffolds produced with more "standard" TPL setups. These steps are useful not only for pushing the resolution beyond the inherent limits of TPL but also for tailoring material properties such as magnetic behavior and mechanical robustness. Two particularly relevant post-processing methods that will be discussed in this section are oxygen plasma treatment and pyrolysis. These approaches address the following challenges: i) reducing structural dimensions beyond the optical resolution limits and ii) enhancing the physical and functional properties of materials.

Oxygen plasma etching is an effective post-processing method used to reduce lateral dimensions and remove residual polymers. In this process, reactive oxygen species interact with organic materials, etching away unpolymerized or loosely bound photoresist and, by providing good control of the etching rate, allowing for fine-tuning of the geometries. The resolution achievable through oxygen plasma etching depends on the geometry of the 3D structure itself. Although a significant reduction of the size is possible, structures can collapse or deform if the thickness is below a critical threshold. This mechanical instability limits the shrinking that can be done without compromising structural integrity. In the literature, several studies have demonstrated the effectiveness of plasma etching for TPL-fabricated structures. $^{[140,204,228,229]}$ For instance, Montemayor et al.[140] combined TPL with oxygen plasma etching, demonstrating the fabrication of 3D hollow metallic nanolattices with features down to 150 nm. In another example by Meza et al.[204] oxygen plasma was combined with conformal coating processes to produce ceramic nanolattices with feature sizes below 100 nm, allowing for the creation of mechanical metamaterials, for which the enhancement in the resolution facilitated the reversible deformation of the structure. Gross et al.[230] combined equiaxed printing trajectories during TPL and oxygen plasma ashing, and realized nanostructures with stable lateral features down to 40 nm, and reported on aspect ratios close to 1 over a range of ashing times.

Another well-established post-processing method is pyrolysis,^[231] a thermally driven process typically carried out in inert or reducing environments. By exposing the polymer

scaffold to high-temperature annealing, the organic components decompose at temperatures typically above ≈600 K, [202] resulting in the transformation into carbon, glassy carbon, or ceramic materials, depending on the initial composition of the photoresist. This method induces isotropic shrinkage-typically by a factor of ≈5-allowing for significant size reduction while preserving the overall geometry. However, if the structure is strongly adhered to the substrate, this shrinkage can cause localized deformation in those regions due to mechanical constraints. Such deformation can be mitigated through the design of an appropriate base for the nanostructure, [61,232] or by the transfer of the printed structure to a new substrate with an anti-sticking coating in order to realize deformation-free pyrolysis of 3D architectures^[233] (Figure 10a,b). Seniutinas et al. showed that pyrolysis and plasma etching can be combined sequentially to achieve better miniaturization of 3D structures, [234] first by isotropic shrinkage via pyrolysis, and then by further fine-tuning the cross-sectional dimensions using oxygen plasma etching, with features as low as 55 nm (Figure 10c-e).

When a TPL scaffold is miniaturized with pyrolysis, there are several routes to creating 3D magnetic nanostructures. Standard physical vapor deposition techniques, such as sputtering, can be used to coat the structure to form a shell-like structure that has been used to realize nano-tripod building blocks, which were subsequently imaged to reveal the stabilization of spin ice vertex configurations, as shown by Pip et al. [61] ALD has also been utilized by Guo et al. [64] to conformally coat a pyrolyzed woodpile, with original lattice periods of 1.5 μm , and then 0.5 μm following pyrolysis. ALD has been used as an intermediate step for coating 3D buckyballs with a conductive Ir layer, followed by Ni electrodeposition, as demonstrated by Gliga et al. [235]

As well as shell-like structures, pyrolysis can also be combined with photoresists that are doped with metallic nanoparticles or metal-containing precursors, [151] as discussed at length in Section 3.4. After the 3D structure is fabricated via TPL, pyrolysis drives off the organic matrix and causes the metal clusters to coalesce, forming a solid metallic architecture with metallic purities as high as 90%. This method has been harnessed by Vyatskikh et al.[151] to fabricate nanolattices with octet geometries made of nanoporous nickel with a high amount of Ni in the final structure, essentially achieving a 3D magnetic nanowire lattice structure (Figure 10f,g). Pyrolysis has also been used to reduce the features of a TPL-fabricated template for electrodeposition by Gunderson et al. [232] (Figure 10h-k), and demonstrated complex Au lattices and linewidths as low as 50 nm, and although magnetic materials were not used in this proof-of-principle work, this demonstrates that combining template-assisted electrodeposition and pyrolysis can leverage the wide scope of available materials with vastly reduced feature sizes.

5. Future Challenges and Opportunities

The convergence of nanoscale additive manufacturing and magnetic materials science is enabling a new era of functional nanomagnetic systems. Among fabrication approaches, TPL stands out for its ability to rapidly generate complex 3D architectures with sub-diffraction resolution, with full freedom over design and with established methods to cast the polymer into one of many available magnetic materials, whilst maintaining a high purity.

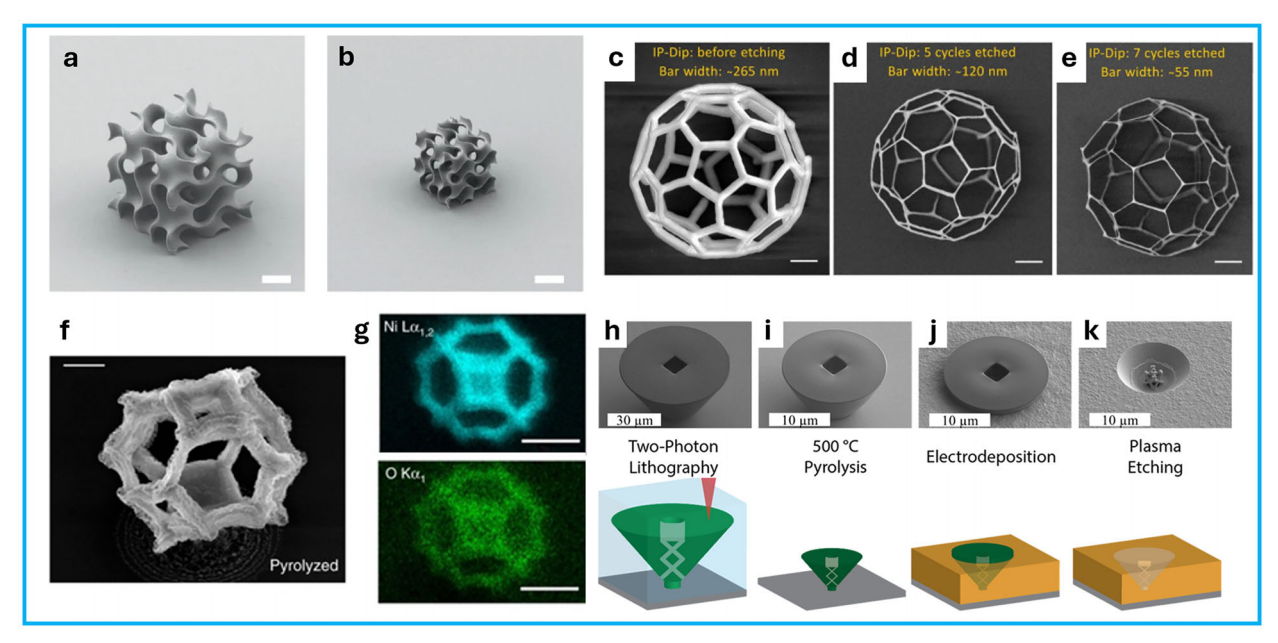


Figure 10. Post-processing examples. a–b) SEM of a gyroid lattice (a) before pyrolysis on original substrate and (b) after pyrolysis on new substrate. Scale bars 20 μm. Reproduced under the terms of the CC-BY 4.0 license. [233] Copyright 2023, The Authors, published by Springer Nature. c–e) Isotropic oxygen plasma etching of polymerized 3D structures: (c) initial buckyball fabricated by TPL, (d) the same buckyball after 5, (e) and 7 etching cycles of isotropic plasma etching. Scale bars 1 μm. Reproduced with permission. [234] Copyright 2018, Elsevier. f) SEM image of supported 20 μm tetrakaidekahedron unit cell on a Si chip fabricated with a Ni-rich photoresist after pyrolysis. Scale bar 1 μm, respectively. g) Corresponding EDS maps showing Ni and O composition throughout the structure. Scale bars 2 μm. Reproduced under the terms of the CC-BY 4.0 license. [151] Copyright 2018, The Authors, published by Springer Nature. h–k) Process flow for the fabrication of nanoscale 3D electroformed samples together with SEM images. Pyrolysis is used to shrink the template patterned with TPL, and subsequently electrodeposition was used to fill the template with metal. Reproduced with permission. [232] Copyright 2021, Wiley.

Moving forward, there are multiple routes to realizing advanced functional devices based upon 3D nanomagnetic architectures. Below, we outline near-term directions that are technically feasible with incremental progress, and longer-term ideas whose payoff is high but require breakthroughs in materials synthesis, processing, and 3D characterization.

5.1. Short-Term Opportunities

5.1.1. Interfacial Stacks on 3D Scaffolds

Summary: Work to date has provided a firm grounding in underlying methods to realize multiple-connected 3D nanomagnetic structures, largely based upon single magnetic materials. A natural progression is the exploration of multilayered and interfacial systems, particularly those exhibiting chiral interactions such as the Dzyaloshinskii–Moriya interaction (DMI). Coating TPL-fabricated networks with heavy-metal/ferromagnet multilayers (e.g., Pt/Co, W/CoFeB) would allow for the stabilization of 3D chiral spin textures such as skyrmions, hopfions, and vortex chains.^[236] These textures are expected to behave differently in curvilinear space, where curved surfaces naturally modify exchange and anisotropy to generate extrinsic Dzyaloshinskii–Moriya-like terms^[52,237,238] and can lead to emergent chirality, even in non-chiral materials.^[239]

Critical barriers: i) Polymer scaffold compatibility has only been characterized with a handful of different deposition

methodologies. [58,64] Interface quality between films deposited on high-curvature TPL features has not been measured in detail. Conventional PVD can yield shadowing. ALD offers conformality but narrows the variety of alloys and often requires hightemperature post-anneals, which can be incompatible with polymer scaffolds. ii) Surface roughness, often in the range of 1-10 nm, [131,144] can produce undesirable orange-peel coupling, [239] change damping, and local anisotropy.^[240] Typical values for TPL fabricated structures are ≈10 nm, [19,84,111] which can be optimized with standard process parameters down to ≈7 nm for individual nanowires^[131,144] and even down to ≈0.4 nm for extended micron-scale ribbons.^[58] Further investigation is required to obtain the low roughness values achieved in traditional CMOS technologies (0.05-0.2 nm). Voxel engineering provides one possibility whilst also providing a route to tuned cross-sectional curvature, allowing for effective DMI and anisotropy terms to be tuning knobs in selecting spin texture within multilayer stacks. The resolution of TPL is also important in the context of magnetic nanostructures and limits the minimum achievable separation between active magnetic nanowires or elements. This has direct implications with respect to controlling dipolar coupling in complex 3D systems or devices.

5.1.2. Low-Power Spin-Orbit Torque Switching

Summary: Achieving low-power spin—orbit torque (SOT) switching of magnetic bits is essential for the development of

addressable 3D spintronic devices, since it allows deterministic control of magnetic states without relying on the larger current densities and Ioule heating provided by spin-transfer torque (STT). STT effects were explored in 3D nanowires with ferromagnetic multilayers obtained by electrodeposition in porous membranes as early as 1999^[241-243] and patented as a 3D fabricated non-volatile magnetic random access memory in 2001.[244] SOT, which arises from spin currents in adjacent heavy metals^[245] is expected to reduce critical thermal effects in spintronics but remains an underexplored phenomenon in 3D systems. 3D structures with graded thickness or local curvature variations could be used to modulate the direction and magnitude of spin accumulation, potentially enabling spatially programmable SOT switching. This is particularly relevant in systems with Rashbatype interfaces, where geometric constraints in TPL-built geometries could break inversion symmetry locally and enhance SOT efficiency.[246]

Critical barriers: i) Reliable electrical contacts. Making reliable electrical contact to 3D magnetic nanostructures and lattices remains a major bottleneck for advancing spintronic functionality beyond the planar limit. Unlike thin films, where contacts can be patterned directly on flat surfaces, 3D architectures introduce curved, elevated, and interconnected geometries that complicate both lithography and metallization. Though several studies[58,247] have demonstrated proof-of-principle approaches, including multi-step lithography to simple wire structures and simple TPL pads to more extended lattices, [248] significant challenges remain. At the level of individual devices, ensuring intimate, low-resistance contact without damaging fragile scaffolds is non-trivial, particularly when conformal coverage of highaspect-ratio features is required. ii) Non-uniform current flow. Though this can be an advantage, as stated above, allowing the control over spin-accumulation, it can also hinder by leading to local hot spots. Thus, controlled SOT, when considering thermal effects, requires advanced design, ideally with full 3D Multiphysics simulation of current mapping.

5.2. Long-Term Opportunities

5.2.1. Beyond Conventional Ferromagnetic Materials

Summary: TPL also offers a route for integrating emerging material classes into 3D magnetic systems. Though there is no work to date, we outline here several promising avenues. Among the most exciting are 2D magnetic materials, [249] whose atomically thin nature and tunable magnetic order make them particularly attractive for conformal integration with 3D scaffolds. For example, a conformal coating of 2D ferromagnetic materials (e.g., Fe₅GeTe₂^[250]) onto TPL scaffolds provides a hybrid platform for coupling spin, valley, or charge transport to 3D magnetic textures. These systems, with their layer-dependent magnetic properties combined with the geometric freedom of 3D design, offer exceptional opportunities for the realization of 3D magnetic metamaterials where intricate functionalities can be enhanced by design. Antiferromagnetic materials^[251] are promising due to their high-speed dynamics and zero net magnetization, making them robust against external fields. 3D nanostructuring may allow for tunable anisotropy, novel domain morphologies, and spin textures unique to these compensated systems. Such materials are also predicted to harbor a family of curvature-driven phenomena^[22] which have not been explored in 3D nanostructured systems, due to constraints on material fabrication. Altermagnets represent a recently identified class of magnetically ordered materials that combine the compensated, zero net magnetization of antiferromagnets with a symmetry-protected spin polarization usually associated with ferromagnets.[252] This arises from their peculiar crystal symmetries (e.g., in MnTe or certain Heuslers), where opposite spin sublattices are not simply related by inversion symmetry. As a result, electronic bands exhibit momentum-dependent spin splitting even though the material as a whole has no macroscopic moment. This "hidden spin polarization" yields highly anisotropic transport properties, including giant anisotropic[253] and direction-dependent spin conductivity.[254] For 3D nanostructured systems, these features open intriguing opportunities. Since spin splitting is symmetryprotected, introducing curvature or designed lattice distortions could engineer the degree and orientation of spin polarization locally via, e.g., non-relativistic spin-orbit coupling or strain, respectively. 3D TPL scaffolds coated with altermagnets might enable direction-sensitive functionalities, such as current rectification or geometry-driven anisotropic spin injection, that a homogeneous and planar material does not provide.

Critical barriers: i) Material growth. Most 2D magnetic materials (e.g., Fe₅GeTe₂, CrI₃) are fabricated by exfoliation or van der Waals epitaxy, both of which are inherently planar. Transferring such materials onto even simple 2.5 or 3D geometries without tearing or unintentionally buckling is a major challenge. Chemical vapor deposition (CVD) routes have shown promise for scalable synthesis, demonstrated in large area growth of layered magnets such as Fe₃GeTe₂, [255] yet the complexity of growing such materials conformally over 3D architectures means achieving uniform coverage around intricate 3D scaffolds and at relatively low temperatures remains uncharted territory. Altermagnets, meanwhile, are at an even earlier stage of development compared to 2D magnets and technologically important antiferromagnets. To date, most altermagnetic compounds such as MnTe and various Heusler alloys have been realized either as bulk single crystals or as epitaxial thin films grown on carefully lattice-matched substrates.[252] These conditions are essential to preserve the crystal symmetries that underpin their symmetry-protected spin splitting and anisotropic transport. However, such requirements make the transition to 3D architectures particularly difficult: epitaxial growth strategies cannot be straightforwardly applied to non-planar scaffolds in general. Conventional bulk synthesis routes provide no obvious route for nanoscale integration. Unlike metallic antiferromagnets, for which sputtering or polycrystalline growth can still yield functional exchange bias, altermagnets appear to demand high crystallographic fidelity,[252] with disorder or strain rapidly suppressing their unique band-structure features. Extending altermagnetic synthesis to scalable, conformal coatings, for example, through non-epitaxial thin-film deposition, chemical methods, or templated growth on amorphous supports, therefore, remains an open long-term challenge. To explore fundamental properties, one might start from altermagnetic 3D shells grown on single-crystalline nanotemplates [36,66,67] and nanomembranes, [256] which offer side facets with engineered lattice constants, which could serve as reference systems



www.afm-journal.de

before exploiting TPL fabricated nanotemplates. Equally important is ensuring that these growth approaches are compatible with CMOS process flows, where temperature budgets are, in general, critical. However, low-temperature processes are already being considered within CMOS to realize stackable 3D transistor systems.^[257]

ii) Role of interfaces. The most technologically important metallic antiferromagnets, such as IrMn, FeMn, PtMn, and NiMn, form the backbone of exchange-bias stacks in magnetic memory and sensor technologies. [258,259] Their functionality relies heavily on achieving the correct crystallographic texture and interfacial order, which typically requires carefully engineered seed layers. For example, IrMn is usually grown on Cu or Pt to stabilize the (111) texture. [260] Translating these stringent growth requirements into 3D geometries is highly non-trivial since curvature may introduce local strain, directly impacting the crystallographic texture, antiferromagnetic ordering, and potentially suppressing interfacial exchange. Finally, such systems often require a high-temperature annealing step, [261] which may damage the polymer support or distort the 3D structure. In such cases, it may be prudent to take advantage of a pyrolysis step in order to realize glassy carbon, which is stable to very high temperatures.[262,263] Here, the high conductivity may also be advantageous for spintronic applications, providing both thermal stability and an electrically active backbone for transport integration.

6. Applications and Outlook

In parallel to fundamental studies, the potential application space for functional 3D nanomagnetism is rapidly expanding. These opportunities can be naturally divided into near-term, medium-term, and long-term horizons, reflecting both the maturity of available material platforms and the challenges of integration. Importantly, the underlying fabrication technologies are progressing toward industrial deployment: two-photon lithography (TPL), once confined to laboratory-scale demonstrations, is now entering manufacturing pipelines in adjacent fields such as micro-optics and photonic packaging, with commercial systems already producing components at scale. This suggests that translation of TPL-based magnetic systems is no longer a purely academic aspiration but increasingly a question of materials compatibility and device integration.

6.1. Near-Term (0-5 years)

Magnetic metamaterials, engineered composites with tailored permeability and anisotropy, can now be realized at the nanoscale using TPL and processing. Such systems are well-suited to act as tunable magnonic crystals and non-reciprocal microwave devices, extending recent advances in planar magnonics into the 3D regime on a chip. [53,264–266] For magnonics, a key challenge is integration with a technologically relevant material such as yttrium iron garnet (YIG), which remains difficult to process in 3D architectures. [264] While ALD of YIG has shown early promise, [267] the absence of lattice-matched $Gd_3Ga_5O_{12}$ (GGG) substrates and corresponding nanotemplates complicates conformal growth. Metallic ferromagnets (e.g., Co, NiFe) and

their multilayers represent practical near-term candidates with larger damping compared to planar YIG, enabling microwave filtering, waveguiding, and on-chip magnonic networks in 3D nanoarchitectures. [264,265] Here, careful control of geometric parameters in complex 3D magnetic lattices such as artificial spinice networks can produce tunable magnonic spectra through controlled vertex populations, providing a pathway to reconfigurable filters operating across the multi-GHz range, relevant to 5G communication technologies. [264]

6.2. Medium-Term (5-10 years)

Thermal spin phenomena, such as the spin Seebeck effect (SSE), offer opportunities to exploit 3D geometries for spatial control of spin current generation and localized energy harvesting. An SSE system such as NiO/Pt^[268] could be embedded into TPL scaffolds, with pyrolyzed glassy carbon frameworks providing both thermal stability and electrical conductivity.[262] Such designs could enable low-power energy harvesting and localized magnetocaloric refrigeration in microscale devices.^[269] Pioneering steps in 3D spin caloritronics have already been achieved in multilayered 3D nanowires fabricated in porous membranes, [270] suggesting that such applications are a realistic medium-term goal, especially once conformal growth techniques upon TPL templates mature. In parallel, 3D nanomagnetic scaffolds decorated with catalytic nanoparticles (for example, via low-cost electrophoretic deposition^[271]) can serve as magnetically switchable catalytic platforms. Under alternating fields, hysteresis-driven nanoscale heating enables selective catalytic activation, [272] a pathway with significant implications for green chemistry and microscale reactors. Magnetic alloys are often used within battery electrodes, yet in these cases, their intrinsic magnetic properties are not exploited. 3D nanostructured electrodes have already been widely investigated^[273] using a variety of fabrication methodologies. We anticipate that combining TPL with electrodeposition will allow for more precise control over geometry and surface area than existing methods.

6.3. Long-Term (10+ years)

Neuromorphic magnetism represents one of the most transformative opportunities. By designing interacting 3D nanomagnetic networks that mimic neuronal connectivity, it is possible to create highly non-linear, history-dependent systems suited to reservoir computing by exploiting the nano-volatile storage capacity of magnets at the same time. Compared to planar architectures, 3D geometries offer vastly increased interconnectivity and state-space, potentially allowing orders-of-magnitude enhancement in computational richness. [274–276] Antiferromagnets represent compelling candidates since their compensated nature suppresses dipolar fields, enabling dense packing, while their THz dynamics allow for ultrafast signal processing. [277] Here, the growth challenges discussed in Section 5 likely limit applications to the long-term future.

Another long-term frontier is magnetomechanical and biomedical platforms. Here, 3D magnetic nanostructures can exert programmable forces on biological systems, allowing for



www.afm-journal.de

stem cell differentiation, $^{[278,279]}$ targeted therapy $^{[280]}$ and remote actuation. $^{[281]}$

In summary, TPL is not only a fabrication tool but a platform for conceptualizing and realizing entirely new classes of 3D nanomagnetic systems. The ability to tailor geometry, couple multiple functionalities, and incorporate advanced materials offers fertile ground for discovery in nanomagnetism and beyond. Continued advances in deposition, post-processing, and characterization will push this field forward, allowing TPL-based magnetic systems to play a key part in next-generation 3D functional materials research.

Acknowledgements

D.G. thanks Swiss National Science Foundation (SNSF) for financial support via grant 197360. S.L. acknowledges funding from the Engineering and Physics Research Council (EPSRC) grant numbers EP/R009147/1 and EP/X0127351/1, and funding from the Leverhulme Trust grant number RPG-2021-139. S.R.-G. acknowledges funding through the Advanced Materials programme supported by MCIN with funding from the European Union NextGenerationEU (PRTR-C17.11) and by the Generalitat de Catalunya and from Spanish MCIN/AEI through Project PID2024-155385NA-C32. C. D. acknowledges funding from the Max Planck Society Lise Meitner Excellence Program and funding from the European Research Council (ERC) under the ERC Starting Grant No. 3DNANOQUANT 101116043.

Conflict of Interest

The authors declare no conflict of interest.

Keywords

3D microstructures, 3D nanomagnetism, 3D nanostructures, artificial spin ice, atomic layer deposition, electrodeposition, electroless deposition, magnetron sputtering, micro-robotics, thermal evaporation, two-photon lithography

Received: June 26, 2025 Revised: October 7, 2025 Published online:

- [1] E. Skliutas, G. Merkininkaite, S. Maruo, W. Zhang, W. Chen, W. Deng, J. Greer, G. V. Freymann, M. Malinauskas, *Nat. Rev. Methods Primers* **2025**, *5*, 1.
- [2] M. Kadic, G. W. Milton, M. van Hecke, M. Wegener, Nat. Rev. Phys. 2019. 1, 198.
- [3] M. Huth, F. Porrati, C. Schwalb, M. Winhold, R. Sachser, M. Dukic, J. Adams, G. Fantner, Beilstein J. Nanotechnol. 2012, 3, 597.
- [4] R. Ma, X. Zhang, D. Sutherland, V. Bochenkov, S. Deng, Int. J. Extrem. Manuf. 2024, 6, 062004.
- [5] V. Reisecker, R. Winkler, H. Plank, Adv. Funct. Mater. 2024, 34, 2407567.
- [6] M. Menétrey, C. Kupferschmid, S. Gerstl, R. Spolenak, Small 2024, 20, 2402067.
- [7] B. Liu, S. Liu, V. Devaraj, Y. Yin, Y. Zhang, J. Ai, Y. Han, J. Feng, Nat. Commun. 2023, 14, 4920.
- [8] S. Ruiz-Gómez, C. Abert, P. Morales-Fernández, C. Fernández-González, S. Koraltan, L. Danesi, D. Suess, M. Varela, G. Sánchez-Santolino, N. Bagués, M. Foerster, M. Á. Niño, A. Mandziak, D.

- Wilgocka-Slezak, P. Nita, M. Koenig, S. Seifert, A. Hierro-Rodriguez, A. Fernández-Pacheco, C. Donnelly, *Nat. Commun.* **2025**, *16*, 7422.
- [9] A. Fernandez-Pacheco, R. Streubel, O. Fruchart, R. Hertel, P. Fischer, R. P. Cowburn, *Nat. Commun.* 2017, 8, 15756.
- [10] A. Fernández-Pacheco, L. Skoric, J. M. De Teresa, J. Pablo-Navarro, M. Huth, O. V. Dobrovolskiy, *Materials (Basel)* **2020**, *13*, 3774.
- [11] C. Vidler, K. Crozier, D. Collins, Microsyst. Nanoeng. 2023, 9, 67.
- [12] G. Lipkowitz, T. Samuelsen, K. Hsiao, B. Lee, M. T. Dulay, I. Coates, H. Lin, W. Pan, G. Toth, L. Tate, E. S. G. Shaqfeh, J. M. DeSimone, Sci. Adv. 2022, 8, abq3917.
- [13] D. Loterie, P. Delrot, C. Moser, Nat. Commun. 2020, 11, 852.
- [14] M. I. Álvarez-Castaño, A. G. Madsen, J. Madrid-Wolff, V. Sgarminato, A. Boniface, J. Glückstad, C. Moser, *Nat. Commun.* 2025, 16, 1551.
- [15] P. Somers, A. Münchinger, S. Maruo, C. Moser, X. Xu, M. Wegener, Nat. Rev. Phys. 2024, 6, 99.
- [16] P. N. Bernal, S. Florczak, S. Inacker, X. Kuang, J. Madrid-Wolff, M. Regehly, S. Hecht, Y. S. Zhang, C. Moser, R. Levato, *Nat. Rev. Mater.* 2025, https://doi.org/10.1038/s41578-025-00785-3.
- [17] V. Hahn, P. Kiefer, T. Frenzel, J. Qu, E. Blasco, C. Barner-Kowollik, M. Wegener, Adv. Funct. Mater. 2020, 30, 1907795.
- [18] Comparing 3D Printers Speed vs Voxel Size, https://3dprintingspeed.aph.kit.edu/ (accessed: August 2025).
- [19] H. Wang, C.-F. Pan, C. Li, K. S. Menghrajani, M. A. Schmidt, A. Li, F. Fan, Y. Zhou, W. Zhang, H. Wang, P. N. S. Nair, J. Y. E. Chan, T. Mori, Y. Hu, G. Hu, S. A. Maier, H. Ren, H. Duan, J. K. W. Yang, Int. J. Extrem. Manuf. 2024, 6, 042002.
- [20] D. Raftrey, A. Hierro-Rodriguez, A. Fernandez-Pacheco, P. Fischer, J. Magn. Magn. Mater. 2022, 563, 169899.
- [21] S. Ladak, A. Fernández-Pacheco, P. Fischer, APL Mater. 2022, 10, 120401.
- [22] D. Makarov, O. M. Volkov, A. Kákay, O. V. Pylypovskyi, B. Budinská, O. V. Dobrovolskiy, Adv. Mater. 2022, 34, 2101758.
- [23] D. D. Sheka, O. V. Pylypovskyi, O. M. Volkov, K. V. Yershov, V. P. Kravchuk, D. Makarov, Small 2022, 18, 2105219.
- [24] G. Binasch, P. Grünberg, F. Saurenbach, W. Zinn, Phys. Rev. B 1989, 39, 4828.
- [25] M. N. Baibich, J. M. Broto, A. Fert, F. N. Van Dau, F. Petroff, P. Etienne, G. Creuzet, A. Friederich, J. Chazelas, *Phys. Rev. Lett.* 1988, 61, 2472.
- [26] N. Locatelli, V. Cros, J. Grollier, Nature Mater 2014, 13, 11.
- [27] C. Chappert, A. Fert, F. N. Van Dau, Nature Mater 2007, 6, 813.
- [28] S. S. P. Parkin, M. Hayashi, L. Thomas, Science 2008, 320, 190.
- [29] S. Parkin, S.-H. Yang, Nat. Nanotechnol. 2015, 10, 195.
- [30] L. Skoric, C. Donnelly, C. Abert, A. Hierro-Rodriguez, D. Suess, A. Fernández-Pacheco, Appl. Phys. Lett. 2021, 118, 242403.
- [31] S. Da Col, S. Jamet, N. Rougemaille, A. Locatelli, T. O. Mentes, B. S. Burgos, R. Afid, M. Darques, L. Cagnon, J. C. Toussaint, O. Fruchart, Phys. Rev. B 2014, 89, 180405.
- [32] S. Da Col, S. Jamet, M. Stano, B. Trapp, S. Le Denmat, L. Cagnon, J. C. Toussaint, O. Fruchart, Appl. Phys. Lett. 2016, 109, 062406.
- [33] L. Gallard, R. Hertel, J. Appl. Phys. 2025, 138, 043907.
- [34] R. Knapman, M. Azhar, A. Pignedoli, L. Gallard, R. Hertel, J. Leliaert, K. Everschor-Sitte, Phys. Rev. B 2025, 111, 134408.
- [35] E. Saavedra, D. Altbir, J. Escrig, S. Castillo-Sepúlveda, R. M. Corona, V. L. Carvalho-Santos, Results in Physics 2024, 62, 107835.
- [36] M. C. Giordano, M. Hamdi, A. Mucchietto, D. Grundler, Phys. Rev. Mater. 2023, 7, 024405.
- [37] R. Hertel, J. Phys.: Condens. Matter 2016, 28, 483002.
- [38] J. A. Fernandez-Roldan, O. Chubykalo-Fesenko, APL Mater. 2022, 10, 111101
- [39] A. Wartelle, B. Trapp, M. Stano, C. Thirion, S. Bochmann, J. Bachmann, M. Foerster, L. Aballe, T. O. Mentes, A. Locatelli, A. Sala, L. Cagnon, J.-C. Toussaint, O. Fruchart, *Phys. Rev. B* 2019, 99, 024433.



- [40] L. Körber, R. Verba, J. A. Otálora, V. Kravchuk, J. Lindner, J. Fassbender, A. Kákay, Phys. Rev. B 2022, 106, 014405.
- [41] F. Brevis, L. Körber, B. Mimica-Figari, R. A. Gallardo, A. Kákay, P. Landeros, Phys. Rev. Appl. 2025, 24, 024058.
- [42] D. D. Sheka, O. V. Pylypovskyi, P. Landeros, Y. Gaididei, A. Kákay, D. Makarov, Commun. Phys. 2020, 3, 128.
- [43] F. Brevis, P. Landeros, J. Lindner, A. Kákay, L. Körber, *Phys. Rev. B* 2024, 110, 134428.
- [44] C. Donnelly, A. Hierro-Rodríguez, C. Abert, K. Witte, L. Skoric, D. Sanz-Hernández, S. Finizio, F. Meng, S. McVitie, J. Raabe, D. Suess, R. Cowburn, A. Fernández-Pacheco, *Nat. Nanotechnol.* 2022, 17, 136.
- [45] D. Sanz-Hernández, A. Hierro-Rodriguez, C. Donnelly, J. Pablo-Navarro, A. Sorrentino, E. Pereiro, C. Magén, S. McVitie, J. M. de Teresa, S. Ferrer, P. Fischer, A. Fernández-Pacheco, ACS Nano 2020, 14, 8084.
- [46] J. Fullerton, N. Leo, J. Jurczyk, C. Donnelly, D. Sanz-Hernández, L. Skoric, N. Mille, S. Stanescu, D. A. MacLaren, R. Belkhou, A. Hierro-Rodriguez, A. Fernández-Pacheco, Adv. Funct. Mater. 2025, https://doi.org/10.1002/adfm.202501615.
- [47] J. Fullerton, C. Phatak, Nano Lett. 2025, 25, 5148.
- [48] A. May, M. Hunt, A. V. D. Berg, A. Hejazi, S. Ladak, Commun. Phys. 2019, 2, 13.
- [49] A. May, M. Saccone, A. van den Berg, J. Askey, M. Hunt, S. Ladak, Nat. Commun. 2021, 12, 3217.
- [50] S. Sahoo, A. May, A. van Den Berg, A. K. Mondal, S. Ladak, A. Barman, *Nano Lett.* 2021, 21, 4629.
- [51] M. Saccone, A. Van den Berg, E. Harding, S. Singh, S. R. Giblin, F. Flicker, S. Ladak, Commun. Phys. 2023, 6, 217.
- [52] R. Streubel, P. Fischer, F. Kronast, V. P. Kravchuk, D. D. Sheka, Y. Gaididei, O. G. Schmidt, D. Makarov, J. Phys. D: Appl. Phys. 2016, 49, 363001.
- [53] G. Gubbiotti, A. Barman, S. Ladak, C. Bran, D. Grundler, M. Huth, H. Plank, G. Schmidt, S. van Dijken, R. Streubel, O. Dobrovoloskiy, V. Scagnoli, L. Heyderman, C. Donnelly, O. Hellwig, L. Fallarino, M. B. Jungfleisch, A. Farhan, N. Maccaferri, P. Vavassori, P. Fischer, R. Tomasello, G. Finocchio, R. Clérac, R. Sessoli, D. Makarov, D. D. Sheka, M. Krawczyk, R. Gallardo, P. Landeros, et al., J. Phys.: Condens. Matter 2025, 37, 143502.
- [54] M. Gołębiewski, H. Reshetniak, U. Makartsou, M. Krawczyk, A. van den Berg, S. Ladak, A. Barman, Phys. Rev. Appl. 2023, 19, 064045.
- [55] M. Gołębiewski, K. Szulc, M. Krawczyk, Acta Mater. 2025, 283, 120499.
- [56] M. Gołębiewski, R. Hertel, M. d'Aquino, V. Vasyuchka, M. Weiler, P. Pirro, M. Krawczyk, S. Fukami, H. Ohno, J. Llandro, ACS Appl. Mater. Interfaces 2024, 16, 22177.
- [57] K. Gu, P. Rigvedi, P. Wang, Z. Yin, H. Deniz, A. Migliorini, S. S. P. Parkin, Adv. Mater. 2025, 37, 2505707.
- [58] A. M. A. Farinha, S.-H. Yang, J. Yoon, B. Pal, S. S. P. Parkin, *Nature* 2025, 639, 67.
- [59] C. Fernández-González, L. Álvaro-Gómez, L. Fernández-García, P. Morales-Fernández, L. Gómez-Cruz, M. W. Khaliq, C. Donnelly, M. Foerster, M. Á. Niño, E. Pereiro, E. Martínez, M. Jaafar, L. Aballe, L. Pérez, S. Ruiz-Gómez, Nano Lett. 2025, 25, 10648.
- [60] C. Donnelly, M. Guizar-Sicairos, V. Scagnoli, M. Holler, T. Huthwelker, A. Menzel, I. Vartiainen, E. Müller, E. Kirk, S. Gliga, J. Raabe, L. J. Heyderman, *Phys. Rev. Lett.* 2015, 114, 115501.
- [61] P. Pip, S. Treves, J. R. Massey, S. Finizio, Z. Luo, A. Hrabec, V. Scagnoli, J. Raabe, L. Philippe, L. J. Heyderman, C. Donnelly, APL Mater. 2022, 10, 101101.
- [62] A. Apseros, V. Scagnoli, M. Holler, M. Guizar-Sicairos, Z. Gao, C. Appel, L. J. Heyderman, C. Donnelly, J. Ihli, *Nature* 2024, 636, 354.
- [63] T. P. Almeida, A. Palomino, S. Lequeux, V. Boureau, O. Fruchart, I. L. Prejbeanu, B. Dieny, D. Cooper, APL Mater. 2022, 10, 061104.

- [64] H. Guo, A. J. M. Deenen, M. Xu, M. Hamdi, D. Grundler, Adv. Mater. 2023, 35, 2303292.
- [65] H. Guo, K. Lenz, M. Gołębiewski, R. Narkowicz, J. Lindner, M. Krawczyk, D. Grundler, arXiv:2506.16103, 2025.
- [66] M. C. Giordano, S. E. Steinvall, S. Watanabe, A. F. Morral, D. Grundler, Nanoscale 2021, 13, 13451.
- [67] M. C. Giordano, K. Baumgaertl, S. Escobar Steinvall, J. Gay, M. Vuichard, A. Fontcuberta i Morral, D. Grundler, ACS Appl. Mater. Interfaces 2020, 12, 40443.
- [68] L. Körber, G. Quasebarth, A. Otto, A. Kákay, AIP Adv. 2021, 11, 095006.
- [69] J. J. Joos, P. Bassirian, P. Gypens, J. Mulkers, K. Litzius, B. Van Waeyenberge, J. Leliaert, J. Appl. Phys. 2023, 134, 171101.
- [70] A. Vansteenkiste, J. Leliaert, M. Dvornik, M. Helsen, F. Garcia-Sanchez, B. Van Waeyenberge, AIP Adv. 2014, 4, 107133.
- [71] M. Beg, M. Lang, H. Fangohr, IEEE Trans. Magn. 2022, 58, 1.
- [72] S. J. R. Holt, M. Lang, J. C. Loudon, T. J. Hicken, D. Suess, D. Cortés-Ortuño, S. A. Pathak, M. Beg, K. Zulfiqar, H. Fangohr, npj Comput. Mater. 2025, 11, 201.
- [73] C. Abert, F. Bruckner, A. Voronov, M. Lang, S. A. Pathak, S. Holt, R. Kraft, R. Allayarov, P. Flauger, S. Koraltan, T. Schrefl, A. Chumak, H. Fangohr, D. Suess, npj Comput. Mater. 2025, 11, 193.
- [74] A. A. Voronov, M. Cuervo Santos, F. Bruckner, D. Suess, A. V. Chumak, C. Abert, npj Spintronics 2025, 3, 19.
- [75] S. Sahoo, S. Mondal, G. Williams, A. May, S. Ladak, A. Barman, *Nanoscale* 2018, 10, 9981.
- [76] M. Bodaghi, L. Wang, F. Zhang, Y. Liu, J. Leng, R. Xing, M. D. Dickey, S. Vanaei, M. Elahinia, S. V. Hoa, D. Zhang, K. Winands, T. Gries, S. Zaman, H. Soleimanzadeh, T. Barsi Palmic, J. Slavic, Y. Tadesse, Q. Ji, C. Zhao, L. Feng, K. Ahmed, M. N. Islam Shiblee, L. Zeenat, F. Pati, L. Ionov, A. Chinnakorn, W. Nuansing, A. M. Sousa, J. Henriques, et al., Smart Mater. Struct. 2024, 33, 113501.
- [77] C. de Marco, C. C. J. Alcântara, S. Kim, F. Briatico, A. Kadioglu, G. de Bernardis, X. Chen, C. Marano, B. J. Nelson, S. Pané, Adv. Mater. Technol. 2019, 4, 1900332.
- [78] C. C. J. Alcântara, S. Kim, S. Lee, B. Jang, P. Thakolkaran, J.-Y. Kim, H. Choi, B. J. Nelson, S. Pané, Small 2019, 15, 1805006.
- [79] X. Hu, I. C. Yasa, Z. Ren, S. R. Goudu, H. Ceylan, W. Hu, M. Sitti, Sci. Adv. 2021, 7, abe8436.
- [80] B. Jian, H. Li, X. He, R. Wang, H. Y. Yang, Q. Ge, Int. J. Extrem. Manuf. 2023, 6, 012001.
- [81] L. Wang, H. Sai, Y.-Y. Tang, B. Li, L. Wang, Y. Yang, K.-C. Yang, P. Lv, H. Duan, T.-Y. Huang, Adv. Funct. Mater. 2025, 35, 2414571.
- [82] P. Kiefer, V. Hahn, M. Nardi, L. Yang, E. Blasco, C. Barner-Kowollik, M. Wegener, Adv. Opt. Mater. 2020, 8, 2000895.
- [83] H. Wang, H. Wang, W. Zhang, J. K. W. Yang, ACS Nano 2020, 14, 10452.
- [84] H. Wang, W. Zhang, D. Ladika, H. Yu, D. Gailevicius, H. Wang, C.-F. Pan, P. N. S. Nair, Y. Ke, T. Mori, J. Y. E. Chan, Q. Ruan, M. Farsari, M. Malinauskas, S. Juodkazis, M. Gu, J. K. W. Yang, Adv. Funct. Mater. 2023, 33, 2214211.
- [85] J. Purtov, A. Verch, P. Rogin, R. Hensel, Microelectron. Eng. 2018, 194, 45.
- [86] T. Koch, W. Zhang, T. T. Tran, Y. Wang, A. Mikitisin, J. Puchhammer, J. R. Greer, A. Ovsianikov, F. Chalupa-Gantner, M. Lunzer, Adv. Mater. 2024, 36, 2308497.
- [87] M. Schmid, D. Ludescher, H. Giessen, Opt. Mater. Express, OME 2019, 9, 4564.
- [88] J. Fischer, M. Wegener, Laser Photonics Rev. 2013, 7, 22.
- [89] X. Zhou, Y. Hou, J. Lin, AIP Adv. 2015, 5, 030701.
- [90] V. Hahn, T. Messer, N. M. Bojanowski, E. R. Curticean, I. Wacker, R. R. Schröder, E. Blasco, M. Wegener, *Nat. Photon.* 2021, 15, 932.
- [91] M. Pawlicki, H. A. Collins, R. G. Denning, H. L. Anderson, Angew. Chem., Int. Ed. 2009, 48, 3244.



www.afm-journal.de

- [92] P. Mueller, M. Thiel, M. Wegener, Opt. Lett. 2014, 39, 6847.
- [93] J. Fischer, M. Wegener, Opt. Mater. Express, OME 2011, 1, 614.
- [94] J. Fischer, J. B. Mueller, A. S. Quick, J. Kaschke, C. Barner-Kowollik, M. Wegener, Adv. Opt. Mater. 2015, 3, 221.
- [95] Z. Gan, Y. Cao, R. A. Evans, M. Gu, Nat. Commun. 2013, 4, 2061.
- [96] J. Fischer, G. von Freymann, M. Wegener, Adv. Mater. 2010, 22, 3578.
- [97] M. He, Z. Zhang, C. Cao, Y. Qiu, X. Shen, G. Zhou, Z. Cai, X. Sun, X. He, L. Xu, X. Liu, C. Ding, Y. Cao, C. Kuang, X. Liu, *PhotoniX* 2022, 3. 25.
- [98] L. Guan, C. Cao, X. Liu, Q. Liu, Y. Qiu, X. Wang, Z. Yang, H. Lai, Q. Sun, C. Ding, D. Zhu, C. Kuang, X. Liu, *Nat. Commun.* 2024, 15, 2387.
- [99] X. Liu, Q. Liu, M. Luo, L. Xu, C. Kuang, X. Liu, Opt. Lett. 2025, 50, 1675.
- [100] T. Tičkūnas, D. Paipulas, V. Purlys, Appl. Phys. Lett. 2020, 116, 031101.
- [101] T. Messer, M. Hippe, J. (Lilyn) Gao, A. Naber, M. Wegener, gxjzz 2024, 5, 269.
- [102] N. M. Bojanowski, A. Vranic, V. Hahn, P. Rietz, T. Messer, J. Brückel, C. Barner-Kowollik, E. Blasco, S. Bräse, M. Wegener, Adv. Funct. Mater. 2023, 33, 2212482.
- [103] A. Mauri, P. Kiefer, P. Neidinger, T. Messer, N. M. Bojanowski, L. Yang, S. Walden, A.-N. Unterreiner, C. Barner-Kowollik, M. Wegener, W. Wenzel, M. Kozlowska, *Chem. Sci.* 2024, 15, 12695.
- [104] X. Liu, C. Ding, X. Gao, X. Shen, M. Tang, Z. Yang, L. Xu, C. Kuang, X. Liu, Opt. Lett. 2023, 48, 4300.
- [105] C. Ding, X. Liu, Q. Liu, D. Zhu, M. Luo, X. Gao, Z. Yang, Q. Sun, Q. Qian, X. Shen, C. Cao, S. You, L. Xu, M. He, Y. Liu, C. Kuang, X. Liu, Laser Photonics Rev. 2024, 18, 2300645.
- [106] J. S. Oakdale, J. Ye, W. L. Smith, J. Biener, Opt. Express 2016, 24, 27077.
- [107] C. Vazquez-Martel, L. Florido Martins, E. Genthner, C. Almeida, A. Martel Quintana, M. Bastmeyer, J. L. Gómez Pinchetti, E. Blasco, Adv. Mater. 2024, 36, 2402786.
- [108] J. Ayestaran, X. L. de Pariza, F. Vidal, C. Vazquez-Martel, A. Pascal, S. Yu, M. Aguirre, A. Nelson, J. R. Leiza, E. Blasco, T. E. Long, R. Aguirresarobe, H. Sardon, Adv. Funct. Mater. 2025, https://doi.org/ 10.1002/adfm.202503712.
- [109] T. Tičkūnas, D. Paipulas, V. Purlys, Opt. Mater. Express, OME 2020, 10, 1432.
- [110] H.-C. Luo, Y.-Y. Zhao, X.-Y. Zhao, Y.-Y. Cao, X.-M. Duan, APL Photonics 2024, 9, 051303.
- [111] T. Aderneuer, O. Fernández, R. Ferrini, Opt. Express 2021, 29, 39511.
- [112] P. Kiefer, V. Hahn, S. Kalt, Q. Sun, Y. M. Eggeler, M. Wegener, *Light: Adv. Manuf.* 2024, 4, 28.
- [113] V. Hahn, P. Rietz, F. Hermann, P. Müller, C. Barner-Kowollik, T. Schlöder, W. Wenzel, E. Blasco, M. Wegener, *Nat. Photon.* 2022, 16, 784.
- [114] P. Somers, Z. Liang, J. E. Johnson, B. W. Boudouris, L. Pan, X. Xu, Light Sci Appl. 2021, 10, 199.
- [115] Z.-X. Liang, Y.-Y. Zhao, J.-T. Chen, X.-Z. Dong, F. Jin, M.-L. Zheng, X.-M. Duan, Nat. Commun. 2025, 16, 2086.
- [116] S. K. Saha, D. Wang, V. H. Nguyen, Y. Chang, J. S. Oakdale, S.-C. Chen, Science 2019, 366, 105.
- [117] W. Ouyang, X. Xu, W. Lu, N. Zhao, F. Han, S.-C. Chen, *Nat. Commun.* 2023, 14, 1716.
- [118] A. Mao, S. Fess, N. Kraiem, P. Li, Z. Wu, Q. Zhu, X. Huang, P. Fan, B. Cui, J.-F. Silvain, S. Hu, M. Anthamatten, S. P. Regan, D. Harding, Y. Lu, Adv. Mater. Technol. 2024, 9, 2400077.
- [119] T. Zandrini, N. Liaros, L. J. Jiang, Y. F. Lu, J. T. Fourkas, R. Osellame, T. Baldacchini, Opt. Mater. Express, OME 2019, 9, 2601.
- [120] P. Rietz, P. Somers, S. Kalt, J. L. G. Schneider, P. Kiefer, M. Wegener, Laser Photonics Rev. 2025, 19, 2500187.

- [121] K. M. Krishnan, Fundamentals and Applications of Magnetic Materials, OUP Oxford, Oxford, United Kingdom 2016.
- [122] G. Scheunert, O. Heinonen, R. Hardeman, A. Lapicki, M. Gubbins, R. M. Bowman, Appl. Phys. Rev. 2016, 3, 011301.
- [123] C. A. Ferguson, D. A. MacLaren, S. McVitie, J. Magn. Magn. Mater. 2015, 381, 457.
- [124] C. Bran, J. A. Fernandez-Roldan, R. P. del Real, A. Asenjo, O. Chubykalo-Fesenko, M. Vazquez, *Nanomaterials* 2021, 11, 600.
- [125] M. Staňo, O. Fruchart, in Handbook of Magnetic Materials (Ed: E. Brück), Elsevier, Amsterdam 2018, 27, pp. 155.
- [126] J. A. Fernandez-Roldan, "Micromagnetism of cylindrical nanowires with compositional and geometric modulations", 2019, https: //repositorio.uam.es/handle/10486/689233 (accessed: September 2022).
- [127] P. Landeros, O. J. Suarez, A. Cuchillo, P. Vargas, Phys. Rev. B 2009, 79, 024404.
- [128] J. Askey, M. Hunt, W. Langbein, S. Ladak, APL Mater. 2022, 10, 071105.
- [129] M. P. Proenca, J. Rial, J. P. Araujo, C. T. Sousa, Sci. Rep. 2021, 11, 10100
- [130] M. Staňo, S. Schaefer, A. Wartelle, M. Rioult, R. Belkhou, A. Sala, T. O. Menteş, A. Locatelli, L. Cagnon, B. Trapp, S. Bochmann, SciPost Physics 2018, 5, 038.
- [131] J. Askey, M. O. Hunt, L. Payne, A. van den Berg, I. Pitsios, A. Hejazi, W. Langbein, S. Ladak, *Nanoscale* 2024, 16, 17793.
- [132] D. D. Sheka, V. P. Kravchuk, Y. Gaididei, J. Phys. A: Math. Theor. 2015, 48, 125202.
- [133] Curvilinear Micromagnetism: From Fundamentals to Applications (Eds: D. Makarov, and D. D. Sheka), 146, Springer, Cham 2022.
- [134] R. M. Bozorth, Ferromagnetism. Piscataway, Wiley-IEEE Press, New Jersev 1993.
- [135] F. T. Z. Toma, M. S. Rahman, K. M. A. Hussain, S. Ahmed, J. Mod. Nanotechnol. 2024, 6.
- [136] A. O. Adeyeye, G. Shimon, in Magnetism of Surfaces, Interfaces, and Nanoscale Materials, vol. 5, (Eds: R. E. Camley, Z. Celinski, R. L. Stamps), Elsevier, North-Holland, 2015, pp. 1–41.
- [137] A. van den Berg, M. Caruel, M. Hunt, S. Ladak, Nano Res. 2022, 16, 1441.
- [138] E. Harding, T. Araki, J. Askey, M. Hunt, A. Van Den Berg, D. Raftrey, L. Aballe, B. Kaulich, E. MacDonald, P. Fischer, S. Ladak, APL Mater. 2024, 12, 021116.
- [139] R. Garg, S. Gonuguntla, S. Sk, M. S. Iqbal, A. O. Dada, U. Pal, M. Ahmadipour, Adv. Colloid Interface Sci. 2024, 330, 103203.
- [140] L. C. Montemayor, L. R. Meza, J. R. Greer, Adv. Eng. Mater. 2014, 16, 184.
- [141] S. Ruiz-Gómez, C. Fernández-González, L. Perez, Micromachines 2022, 13, 1223.
- [142] A. Pasa, M. Munford, in Encyclopedia of Chemical Processing, Dekker Encyclopedias, no. 2, New York, 2006, pp. 821–832, http://fisica. ufmt.br/escola/old-2005/material/pasa.pdf (accessed: July 2018).
- [143] G. Williams, M. Hunt, B. Boehm, A. May, M. Taverne, D. Ho, S. Giblin, D. Read, J. Rarity, R. Allenspach, S. Ladak, *Nano Res.* 2018, 11, 845.
- [144] J. Askey, M. O. Hunt, W. Langbein, S. Ladak, *Nanomaterials* 2020, 10, 429.
- [145] R. Muraliraja, R. Anthoni Sagaya Selvan, A. Selvakumar, M. Franco, T. R. Tamilarasan, U. Sanjith, W. Sha, J. Sudagar, J. Alloys Compd. 2023, 960, 170723.
- [146] J. Sudagar, J. Lian, W. Sha, J. Alloys Compd. 2013, 571, 183.
- [147] C. A. Loto, Silicon 2016, 8, 177.
- [148] T. Zandrini, S. Taniguchi, S. Maruo, Micromachines 2017, 8, 35.
- [149] P. Pip, C. Donnelly, M. Döbeli, C. Gunderson, L. J. Heyderman, L. Philippe, Small 2020, 16, 2004099.



- [150] T. Jussila, A. Philip, T. Tripathi, K. Nielsch, M. Karppinen, *Appl. Phys. Rev.* 2023, 10, 041313.
- [151] A. Vyatskikh, S. Delalande, A. Kudo, X. Zhang, C. M. Portela, J. R. Greer, Nat. Commun. 2018, 9, 593.
- [152] I. A. Paun, B. S. Calin, C. C. Mustaciosu, M. Mihailescu, A. Moldovan, O. Crisan, A. Leca, C. R. Luculescu, *Materials* 2019, 12, 2834
- [153] M. Malekzadeh, M. T. Swihart, Chem. Soc. Rev. 2021, 50, 7132.
- [154] B. Janarthanan, C. Thirunavukkarasu, S. Maruthamuthu, M. A. Manthrammel, M. Shkir, S. AlFaify, M. Selvakumar, V. R. M. Reddy, C. Park, J. Mol. Struct. 2021, 1241, 130606.
- [155] J. Hora, C. Hall, D. Evans, E. Charrault, Adv. Eng. Mater. 2018, 20, 1700868.
- [156] S. Kim, F. Qiu, S. Kim, A. Ghanbari, C. Moon, L. Zhang, B. J. Nelson, H. Choi, Adv. Mater. 2013, 25, 5863.
- [157] S. Tottori, L. Zhang, F. Qiu, K. K. Krawczyk, A. Franco-Obregón, B. J. Nelson, Adv. Mater. 2012, 24, 811.
- [158] R. Streubel, D. Makarov, F. Kronast, V. Kravchuk, M. Albrecht, O. G. Schmidt, Phys. Rev. B 2012, 85, 174429.
- [159] A. A. Serga, A. V. Chumak, B. Hillebrands, J. Phys. D: Appl. Phys. 2010, 43, 264002.
- [160] J. Barker, G. E. W. Bauer, Phys. Rev. Lett. 2016, 117, 217201.
- [161] T. Schneider, A. A. Serga, B. Leven, B. Hillebrands, R. L. Stamps, M. P. Kostylev, *Appl. Phys. Lett.* **2008**, *92*, 022505.
- [162] J. Li, X. Li, T. Luo, R. Wang, C. Liu, S. Chen, D. Li, J. Yue, S.-H. Cheng, D. Sun, Sci. Rob. 2018, 3, aat8829.
- [163] M. Hunt, M. Taverne, J. Askey, A. May, A. Van Den Berg, Y-L. D. Ho, J. Rarity, S. Ladak, *Materials* 2020, 13, 761.
- [164] F. Meng, C. Donnelly, L. Skoric, A. Hierro-Rodriguez, J. Liao, A. Fernández-Pacheco, Micromachines 2021, 12, 859.
- [165] T.-Y. Huang, M. S. Sakar, A. Mao, A. J. Petruska, F. Qiu, X.-B. Chen, S. Kennedy, D. Mooney, B. J. Nelson, Adv. Mater. 2015, 27, 6644.
- [166] S. Puce, E. Sciurti, F. Rizzi, B. Spagnolo, A. Qualtieri, M. De Vittorio, U. Staufer, Micro and Nano Engineering 2019, 2, 70.
- [167] V. Linder, B. D. Gates, D. Ryan, B. A. Parviz, G. M. Whitesides, Small 2005, 1, 730.
- [168] A. Van Den Berg, Exploring the Physics of 3D Magnetic Nanowires and 3D Artificial Spin-ice Lattices Phd, Cardiff University, United Kingdom 2022
- [169] D. A. Bograchev, T. B. Kabanova, A. D. Davydov, J. Solid State Electrochem. 2025, 29, 1309.
- [170] J. Wang, Y. Zhou, L. Jiang, ACS Nano 2021, 15, 18974.
- [171] J. Duan, J. Liu, T. W. Cornelius, H. Yao, D. Mo, Y. Chen, L. Zhang, Y. Sun, M. Hou, C. Trautmann, R. Neumann, Nuclear Instruments and Methods in Physics Research Section B: Beam Interactions with Materials and Atoms 2009, 267, 2567.
- [172] K. V. Frolov, D. L. Zagorskii, I. S. Lyubutin, V. V. Korotkov, S. A. Bedin, S. N. Sulyanov, V. V. Artemov, B. V. Mchedlishvili, *JETP Lett.* 2014, 99, 570.
- [173] Y. Chen, J. Duan, H. Yao, D. Mo, T. Wang, Y. Sun, J. Liu, J. Wuhan Univ. Technol.-Mat. Sci. Edit. 2015, 30, 665.
- [174] T. Ohgai, X. Hoffer, L. Gravier, J.-E. Wegrowe, J.-P. Ansermet, Nanotechnology 2003, 14, 978.
- [175] T. Ohgai, K. Hjort, R. Spohr, R. Neumann, J. Appl. Electrochem. 2008, 38, 713.
- [176] C. Fernández-González, J. C. Guzmán-Mínguez, A. Guedeja-Marrón, E. García-Martín, M. Foerster, M. Á. Niño, L. Aballe, A. Quesada, L. Pérez, S. Ruiz-Gómez, *Nanomaterials* 2021, 11, 1657.
- [177] C. Bran, E. Berganza, E. M. Palmero, J. A. Fernandez-Roldan, R. P. Del Real, L. Aballe, M. Foerster, A. Asenjo, A. Fraile Rodríguez, M. Vazquez, J. Mater. Chem. C 2016, 4, 978.
- [178] J. A. Fernandez-Roldan, A. De Riz, B. Trapp, C. Thirion, M. Vazquez, J.-C. Toussaint, O. Fruchart, D. Gusakova, Sci. Rep. 2019, 9, 5130.

- [179] C. Bran, Y. P. Ivanov, J. Kosel, O. Chubykalo-Fesenko, M. Vazquez, Nanotechnology 2017, 28, 095709.
- [180] C. Bran, J. A. Fernandez-Roldan, R. P. Del Real, A. Asenjo, Y.-S. Chen, J. Zhang, X. Zhang, A. Fraile Rodríguez, M. Foerster, L. Aballe, O. Chubykalo-Fesenko, M. Vazquez, ACS Nano 2020, 14, 12819.
- [181] E. Berganza, M. Jaafar, C. Bran, J. A. Fernández-Roldán, O. Chubykalo-Fesenko, M. Vázquez, A. Asenjo, Sci. Rep. 2017, 7, 11576.
- [182] A. Ruiz-Clavijo, S. Ruiz-Gomez, O. Caballero-Calero, L. Perez, M. Martin-Gonzalez, physica status solidi (RRL) – Rapid Research Letters 2019, 13, 1900263.
- [183] S. Ruiz-Gómez, C. Fernández-González, E. Martínez, V. Raposo, A. Sorrentino, M. Foerster, L. Aballe, A. Mascaraque, S. Ferrer, L. Pérez, Nanoscale 2020, 12, 17880.
- [184] P. Schürch, R. Ramachandramoorthy, L. Pethö, J. Michler, L. Philippe, Appl. Mater. Today 2020, 18, 100472.
- [185] H. Shen, S. Cai, Z. Wang, Z. Ge, W. Yang, Mater. Des. 2023, 227, 111735.
- [186] M. A. Zeeshan, R. Grisch, E. Pellicer, K. M. Sivaraman, K. E. Peyer, J. Sort, B. Özkale, M. S. Sakar, B. J. Nelson, S. Pané, Small 2014, 10, 1284.
- [187] C. C. J. Alcântara, F. C. Landers, S. Kim, C. De Marco, D. Ahmed, B. J. Nelson, S. Pané, Nat. Commun. 2020, 11, 5957.
- [188] J. A. Fernandez-Roldan, R. P. del Real, C. Bran, M. Vazquez, O. Chubykalo-Fesenko, *Nanoscale* 2018, 10, 5923.
- [189] P. Schürch, L. Pethö, J. Schwiedrzik, J. Michler, L. Philippe, Adv. Mater. Technol. 2018, 3, 1800274.
- [190] N. K. Kim, S. M. Kang, T. Kim, S. Kim, G. H. Kim, Adv. Mater. Interfaces 2025, 12, 2400931.
- [191] S. S. Djokić, P. L. Cavallotti, in *Electrodeposition: Theory and Practice*, (Ed: S. S. Djokic), Springer, New York, NY 2010, pp. 251–289.
- [192] J. K. Pancrecious, S. B. Ulaeto, R. Ramya, T. P. D. Rajan, B. C. Pai, Int. Mater. Rev. 2018, 63, 488.
- [193] D. Tiwari, M. C. Scheuerlein, M. Jaber, E. Gautier, L. Vila, J.-P. Attané, M. Schöbitz, A. Massebouf, T. Hellmann, J. P. Hofmann, W. Ensinger, O. Fruchart, J. Magn. Magn. Mater. 2023, 575, 170715
- [194] M. D. L. Balela, S. Yagi, E. Matsubara, Electrochem. Solid-State Lett. 2011, 14, D68.
- [195] M. Kawamori, S. Yagi, E. Matsubara, J. Electrochem. Soc. 2011, 158, E79.
- [196] A. I. Aristov, M. Manousidaki, A. Danilov, K. Terzaki, C. Fotakis, M. Farsari, A. V. Kabashin, Sci. Rep. 2016, 6, 25380.
- [197] S. Papamakarios, O. Tsilipakos, I. Katsantonis, A. D. Koulouklidis, M. Manousidaki, G. Zyla, C. Daskalaki, S. Tzortzakis, M. Kafesaki, M. Farsari, ACS Photonics 2025, 12, 87.
- [198] G. Zyla, S. Papamakarios, D. C. Zografopoulos, A. Christoforidou, G. Kenanakis, M. Farsari, O. Tsilipakos, Adv. Mater. Technol. 2025, 10. 2402137.
- [199] M. Mieszala, M. Hasegawa, G. Guillonneau, J. Bauer, R. Raghavan, C. Frantz, O. Kraft, S. Mischler, J. Michler, L. Philippe, Small 2017, 13, 1602514.
- [200] R. Bernasconi, G. Prioglio, C. C. J. Alcantara, S. Panè, L. Magagnin, in 2021 21st International Conference on Solid-State Sensors, Actuators and Microsystems (Transducers), IEEE, Orlando, FL 2021, pp. 369– 372
- [201] (Ed: C. S. Hwang), Atomic Layer Deposition for Semiconductors, Springer, New York Heidelberg Dordrecht London 2014.
- [202] Y. Liu, H. Wang, J. Ho, R. C. Ng, R. J. H. Ng, V. H. Hall-Chen, E. H. H. Koay, Z. Dong, H. Liu, C.-W. Qiu, J. R. Greer, J. K. W. Yang, Nat. Commun. 2019, 10, 4340.
- [203] H. C. Nallan, X. Yang, B. M. Coffey, J. G. Ekerdt, Journal of Vacuum Science & Technology A 2022, 40, 062406.
- [204] L. R. Meza, S. Das, J. R. Greer, Science 2014, 345, 1322.



- [205] B. Quinard, F. Godel, M. Galbiati, V. Zatko, A. Sander, A. Vecchiola, S. Collin, K. Bouzehouane, F. Petroff, R. Mattana, M.-B. Martin, B. Dlubak, P. Seneor, Appl. Phys. Lett. 2022, 120, 213503.
- [206] H. Plank, R. Winkler, C. H. Schwalb, J. Hütner, J. D. Fowlkes, P. D. Rack, I. Utke, M. Huth, Micromachines 2020, 11, 48.
- [207] R. C. Popescu, B. S. Calin, E. Tanasa, E. Vasile, M. Mihailescu, I. A. Paun, Front. Bioeng. Biotechnol. 2023, 11, 1273277.
- [208] Y. Lin, J. Xu, Adv. Opt. Mater. 2018, 6, 1701359.
- [209] M. Carlotti, V. Mattoli, Small 2019, 15, 1902687.
- [210] X. Liang, Z. Chen, Y. Deng, D. Liu, X. Liu, Q. Huang, T. Arai, Cyborg and Bionic Systems 2023, 4, 0009.
- [211] C. A. Spiegel, M. Hippler, A. Münchinger, M. Bastmeyer, C. Barner-Kowollik, M. Wegener, E. Blasco, Adv. Funct. Mater. 2020, 30, 1907615.
- [212] L. Pertoldi, V. Zega, C. Comi, R. Osellame, J. Appl. Phys. 2020, 128, 175102.
- [213] Nanoscribe, IP Photoresin DataSheets, https://www.nanoscribe.com/en/products/ip-photoresins/ (accessed: September 2025).
- [214] UpNano, UpNano standard production datasheets, https://www. upnano.com/standard-production/ (accessed: September 2025).
- [215] P. Mainik, C. A. Spiegel, E. Blasco, Adv. Mater. 2024, 36, 2310100.
- [216] N. Geid, A. Husari, E. Galli, L. Leffler, P. Tomakidi, J. Rühe, Adv. Funct. Mater. 2025, 35, 2419614.
- [217] N. Geid, J. U. Leutner, O. Prucker, J. Rühe, Actuators 2023, 12, 124.
- [218] F. Rajabasadi, L. Schwarz, M. Medina-Sánchez, O. G. Schmidt, Prog. Mater. Sci. 2021, 120, 100808.
- [219] C. Peters, O. Ergeneman, P. D. W. García, M. Müller, S. Pané, B. J. Nelson, C. Hierold, Adv. Funct. Mater. 2014, 24, 5269.
- [220] M. Suter, L. Zhang, E. C. Siringil, C. Peters, T. Luehmann, O. Ergeneman, K. E. Peyer, B. J. Nelson, C. Hierold, Biomed. Microdevices 2013, 15, 997.
- [221] J. Giltinan, V. Sridhar, U. Bozuyuk, D. Sheehan, M. Sitti, Advanced Intelligent Systems 2021, 3, 2000204.
- [222] S. Peng, X. Lei, S. Sun, Y. Zhu, J. Qiu, H. Yang, Adv. Eng. Mater. 2024, 26, 2301960.
- [223] L. Yang, X. Chen, L. Wang, Z. Hu, C. Xin, M. Hippler, W. Zhu, Y. Hu, J. Li, Y. Wang, L. Zhang, D. Wu, J. Chu, Adv. Funct. Mater. 2019, 29, 1905745
- [224] H. Xia, J. Wang, Y. Tian, Q.-D. Chen, X.-B. Du, Y.-L. Zhang, Y. He, H.-B. Sun, Adv. Mater. **2010**, *22*, 3204.
- [225] C. Zheng, F. Jin, Y. Zhao, M. Zheng, J. Liu, X. Dong, Z. Xiong, Y. Xia, X. Duan, Sens. Actuators, B 2020, 304, 127345.
- [226] R. Li, M. Jiang, B. Liu, S. Jiang, C. Chen, M. Liang, L. Qu, C. Wang, G. Zhao, Y. Hu, D. Wu, J. Chu, J. Li, Lab Chip 2024, 24, 832.
- [227] Y. Wang, C. Yi, W. Tian, F. Liu, G. J. Cheng, Nat. Mater. 2024, 23, 1645.
- [228] J. M. Elorrieta, G. Mathew, C. Garcia-Sacristán, L. Martegiani, R. García, E. Berganza, Social Science Research Network 2025, 5217649.
- [229] M. Power, A. Barbot, F. Seichepine, G.-Z. Yang, Advanced Intelligent Systems 2023, 5, 2200121.
- [230] A. J. Gross, K. Bertoldi, Small 2019, 15, 1902370.
- [231] B. Cardenas-Benitez, C. Eschenbaum, D. Mager, J. G. Korvink, M. J. Madou, U. Lemmer, I. D. Leon, S. O. Martinez-Chapa, *Microsyst. Nanoeng.* 2019, 5, 38.
- [232] C. Gunderson, N. Rohbeck, M. Tranchant, J. Michler, L. Philippe, Adv. Eng. Mater. 2021, 23, 2001293.
- [233] T. Mori, H. Wang, W. Zhang, C. C. Ser, D. Arora, C.-F. Pan, H. Li, J. Niu, M. A. Rahman, T. Mori, H. Koishi, J. K. W. Yang, *Nat. Commun.* 2023, 14, 5876.
- [234] G. Seniutinas, A. Weber, C. Padeste, Microelectron. Eng. 2018, 191, 25.
- [235] S. Gliga, G. Seniutinas, A. Weber, C. David, *Mater. Today* **2019**, *26*, 100
- [236] R. Wiesendanger, Nat. Rev. Mater. 2016, 1, 16044.

- [237] Y. Gaididei, V. P. Kravchuk, D. D. Sheka, Phys. Rev. Lett. 2014, 112, 257203.
- [238] V. P. Kravchuk, U. K. Rößler, O. M. Volkov, D. D. Sheka, J. van den Brink, D. Makarov, H. Fuchs, H. Fangohr, Y. Gaididei, *Phys. Rev. B* 2016, 94, 144402.
- [239] M. A. Kuznetsov, O. G. Udalov, A. A. Fraerman, J. Magn. Magn. Mater. 2019, 474, 104.
- [240] S. Ingvarsson, L. Ritchie, X. Y. Liu, G. Xiao, J. C. Slonczewski, P. L. Trouilloud, R. H. Koch, *Phys. Rev. B* **2002**, *66*, 214416.
- [241] J.-E. Wegrowe, D. Kelly, Y. Jaccard, P. Guittienne, J.-P. Ansermet, Europhys. Lett. 1999, 45, 626.
- [242] D. Kelly, J.-E. Wegrowe, T. Truong, X. Hoffer, J.-P. Ansermet, *Phys. Rev. B* 2003, 68, 134425.
- [243] H. Yu, S. Granville, D. P. Yu, J.-P. Ansermet, Phys. Rev. Lett. 2010, 104, 146601.
- [244] J.-E. Wegrowe, J.-P. Ansermet, S. E. Gilbert, Non-volatile magnetic random access memory, 2001, https://infoscience.epfl.ch/handle/ 20.500.14299/138394.
- [245] A. Manchon, J. Zelezný, I. M. Miron, T. Jungwirth, J. Sinova, A. Thiaville, K. Garello, P. Gambardella, Rev. Mod. Phys. 2019, 91, 035004.
- [246] I. M. Miron, K. Garello, G. Gaudin, P.-J. Zermatten, M. V. Costache, S. Auffret, S. Bandiera, B. Rodmacq, A. Schuhl, P. Gambardella, *Nature* 2011, 476, 189.
- [247] F. Meng, C. Donnelly, C. Abert, L. Skoric, S. Holmes, Z. Xiao, J.-W. Liao, P. J. Newton, C. H. W. Barnes, D. Sanz-Hernández, A. Hierro-Rodriguez, D. Suess, R. P. Cowburn, A. Fernández-Pacheco, ACS Nano 2021, 15, 6765.
- [248] C. Kern, M. Kadic, M. Wegener, Phys. Rev. Lett. 2017, 118, 016601.
- [249] M. Gibertini, M. Koperski, A. F. Morpurgo, K. S. Novoselov, Nat. Nanotechnol. 2019, 14, 408.
- [250] M. Ribeiro, G. Gentile, A. Marty, D. Dosenovic, H. Okuno, C. Vergnaud, J.-F. Jacquot, D. Jalabert, D. Longo, P. Ohresser, A. Hallal, M. Chshiev, O. Boulle, F. Bonell, M. Jamet, npj 2D Mater. Appl. 2022, 6. 10.
- [251] T. Jungwirth, X. Marti, P. Wadley, J. Wunderlich, Nature Nanotech 2016, 11, 231.
- [252] L. Bai, W. Feng, S. Liu, L. Šmejkal, Y. Mokrousov, Y. Yao, Adv. Funct. Mater. 2024, 34, 2409327.
- [253] R. D. Gonzalez Betancourt, J. Zubáč, K. Geishendorf, P. Ritzinger, B. Ruzicková, T. Kotte, J. Zelezný, K. Olejník, G. Springholz, B. Büchner, A. Thomas, K. Výborný, T. Jungwirth, H. Reichlová, D. Kriegner, npj Spintronics 2024. 2, 45.
- [254] H.-Z. Zhang, C. Cui, J. Duan, T. He, R.-W. Zhang, Mater. Horiz. 2025.
- [255] H. Ren, M. Lan, Molecules 2023, 28, 7244.
- [256] M. Friedl, K. Cerveny, P. Weigele, G. Tütüncüoglu, S. Martí-Sánchez, C. Huang, T. Patlatiuk, H. Potts, Z. Sun, M. O. Hill, L. Güniat, W. Kim, M. Zamani, V. G. Dubrovskii, J. Arbiol, L. J. Lauhon, D. M. Zumbühl, A. Fontcuberta i Morral, *Nano Lett.* 2018, 18, 2666
- [257] J. Franco, H. Arimura, J.-F. de Marneffe, S. Brus, R. Ritzenthaler, E. D. Litta, K. Croes, B. Kaczer, N. Horiguchi, in 2023 IEEE Symposium on VLSI Technology and Circuits (VLSI Technology and Circuits), IEEE, Rihga Royal Hotel, Kyoto, Japan, 2023, pp. 1–2.
- [258] J. Nogués, I. K. Schuller, J. Magn. Magn. Mater. 1999, 192, 203.
- [259] T. Blachowicz, A. Ehrmann, M. Wortmann, Nanomaterials 2023, 13, 2418.
- [260] I. L. Castro, V. P. Nascimento, E. C. Passamani, A. Y. Takeuchi, C. Larica, M. Tafur, F. Pelegrini, J. Appl. Phys. 2013, 113, 203903.
- [261] G. Vallejo-Fernandez, T. Dimopoulos, M. Ruehrig, K. O'Grady, J. Magn. Magn. Mater. 2007, 310, 786.
- [262] V. Uskoković, Carbon Trends 2021, 5, 100116.
- [263] P. R. Onffroy, S. Chiovoloni, H. L. Kuo, M. A. Saccone, J. Q. Lu, J. M. DeSimone, JACS Au 2024, 4, 3706.



- [264] A. Barman, G. Gubbiotti, S. Ladak, A. O. Adeyeye, M. Krawczyk, J. Gräfe, C. Adelmann, S. Cotofana, A. Naeemi, V. I. Vasyuchka, B. Hillebrands, J. Phys.: Condens. Matter 2021, 33, 413001.
- [265] B. Flebus, D. Grundler, B. Rana, Y. Otani, I. Barsukov, A. Barman, G. Gubbiotti, P. Landeros, J. Akerman, U. Ebels, P. Pirro, J. Phys.: Condens. Matter 2024, 36, 363501.
- [266] M. Xu, A. J. M. Deenen, H. Guo, D. Grundler, arXiv: 2404.19153.
- [267] M. Lammel, D. Scheffler, D. Pohl, P. Swekis, S. Reitzig, S. Piontek, H. Reichlova, R. Schlitz, K. Geishendorf, L. Siegl, B. Rellinghaus, L. M. Eng, K. Nielsch, S. T. B. Goennenwein, A. Thomas, *Phys. Rev. Mater.* 2022, 6, 044411.
- [268] P. R. T. Ribeiro, F. L. A. Machado, M. Gamino, A. Azevedo, S. M. Rezende, *Phys. Rev. B* 2019, 99, 094432.
- [269] J. H. Belo, A. L. Pires, J. P. Araújo, A. M. Pereira, J. Mater. Res. 2019, 34, 134.
- [270] G. E. W. Bauer, E. Saitoh, B. J. van Wees, Nature Mater 2012, 11, 391.
- [271] L. Besra, M. Liu, Prog. Mater. Sci. 2007, 52, 1.
- [272] A. Bordet, W. Leitner, B. Chaudret, Angew. Chem., Int. Ed. 2025, 64, 202424151.

- [273] H. Zhao, Y. Lei, Adv. Energy Mater. 2020, 10, 2001460.
- [274] S. J. Kim, H.-J. Lee, C.-H. Lee, H. W. Jang, npj 2D Mater. Appl. 2024, 8. 70.
- [275] D. Bhattacharya, C. Langton, M. M. Rajib, E. Marlowe, Z. Chen, W. Al Misba, J. Atulasimha, X. Zhang, G. Yin, K. Liu, ACS Appl. Mater. Interfaces 2025, 17, 20087.
- [276] T. Dion, K. D. Stenning, A. Vanstone, H. H. Holder, R. Sultana, G. Alatteili, V. Martinez, M. T. Kaffash, T. Kimura, R. F. Oulton, W. R. Branford, H. Kurebayashi, E. Iacocca, M. B. Jungfleisch, J. C. Gartside, Nat. Commun. 2024, 15, 4077.
- [277] A. Kurenkov, S. Fukami, H. Ohno, J. Appl. Phys. 2020, 128, 010902.
- [278] Z. Ebrahimi, S. Irani, A. Ardeshirylajimi, E. Seyedjafari, *Sci. Rep.* 2022, 12, 12359.
- [279] V. Du, N. Luciani, S. Richard, G. Mary, C. Gay, F. Mazuel, M. Reffay, P. Menasché, O. Agbulut, C. Wilhelm, Nat. Commun. 2017, 8, 400.
- [280] W. Gao, D. Kagan, O. S. Pak, C. Clawson, S. Campuzano, E. Chuluun-Erdene, E. Shipton, E. E. Fullerton, L. Zhang, E. Lauga, J. Wang, Small 2012, 8, 460.
- [281] M. Rotherham, T. Nahar, T. J. Broomhall, N. D. Telling, A. J. El Haj, Curr. Opin. Biomed. Eng. 2022, 24, 100410.



Joseph Askey received his BSc (2017) from University of Bristol, MSc (2018) and Ph.D. (2023) in Physics from Cardiff University. He is currently working as a postdoctoral research associate at Cardiff University with a focus on the fabrication, characterisation and modelling of 3D magnetic and thermoelectric metamaterials.



Arjen van den Berg received his Ph.D. under Prof Sam Ladak at Cardiff University in 2023, where he resides as a postdoctoral research associate. His research interests revolve around 3D magnetic nanostructures with a particular focus on ordering in 3D artificial spin ice systems.



Sandra Ruiz Gomez is currently the Head of the X-ray & TEM Interfaces Group at the ALBA Synchrotron. She received her Ph.D. in Physics from the Universidad Complutense de Madrid in 2019. Her current research interests focus on the fabrication and study of three-dimensional magnetic nanostructures, as well as the development of new tools for correlative TEM/X-ray magnetic microscopy.



Claire Donnelly is currently an independent group leader at the Max Planck Institute for Chemical Physics of Solids in Dresden, Germany, where she leads her group Spin3D. Her research interests span three dimensional magnetic and quantum nanomaterials. She and her group develop advanced fabrication and X-ray magnetic microscopy techniques to probe these three dimensional nanosystems experimentally.



Dirk Grunder received his diploma (physics) from Universität Hamburg (UHH), Germany, in 1991. Work on superconducting devices at the Philips Research Laboratories, Hamburg, he obtained the ScD degree in 1995 from UHH. As a permanent researcher he worked on semiconductors and spintronics from 1995 to 2005 at the Institute of Physics of UHH. He received his habilitation in experimental physics in 2001. His current interest is in atomic layer deposition of ferromagnetic metals and superconductors for 3D nanomagnonics and super-spintronics.



Sam Ladak is a Professor of Physics at Cardiff University, UK, where he leads research into threedimensional (3D) nanomagnetism and functional magnetic metamaterials. His work explores the use of advanced fabrication methods, with emphasis on two-photon lithography, to realize complex 3D magnetic systems with tailored geometry and topology. Combining experiment and simulation his group investigates magnetic phenomena in artificial spin ices, magnetic nanowires and magnonic networks.